Electronic Supplementary Material (ESI) for Journal of Materials Chemistry A.

SUPPORTING INFORMATION

Hydrated Alkali-$B_{11}H_{14}$ Salts as Potential Solid-State Electrolytes

Diego H. P. Souza,[a] Kasper T. Møller,[a,b] Stephen A. Moggach,[c] Terry D. Humphries,[a] Anita M. D'Angelo,[d] Craig E. Buckley,[a] and Mark Paskevicius[a*]

[a.] Department of Physics and Astronomy, Fuels and Energy Technology Institute, Curtin University, GPO Box U1987, Perth, WA 6845, Australia.

[b.] Department of Biological and Chemical Engineering, Aarhus University, Aabogade 40, Aarhus, DK-8200, Denmark.

[c.] School of Molecular Sciences, The University of Western Australia (M310), Crawley, WA 6009, Australia; Centre for Microscopy, Characterization and Analysis, The University of Western Australia, Perth, WA 6009, Australia.

[d.] Australian Synchrotron (ANSTO), Clayton, VIC 3168, Australia

Corresponding Author

E-mail: m.paskevicius@curtin.edu.au

EXPERIMENTAL DETAILS

Nuclear Magnetic Resonance

Nuclear Magnetic Resonance (NMR) spectra were collected on a Bruker Avance III 400 MHz NanoBay spectrometer (^{1}H: 400 MHz, ^{11}B: 128 MHz, ^{11}B{^{1}H}: 128 MHz) at room temperature. The powdered samples were dissolved in 600 μL of deuterated solvent (D_2O, DMSO-*d*$_6$ or CD_3CN) prior to analysis. The ^{11}B spectra were referenced to a boron trifluoride etherate ($BF_3O(C_2H_5)_2$) external standard, and the ^{1}H spectra were referenced to a tetramethylsilane ($Si(CH_3)_4$) external standard.

Fourier Transformed Infrared Spectroscopy

Fourier Transformed Infrared Spectroscopy (FTIR) was conducted on a Thermoscientific Summit ATR spectrometer. Data was measured between 500 − 4000 cm^{-1} with a spectral resolution of 4 cm^{-1}. A total of 16 scans were collected and averaged per sample. The samples had to be briefly exposed to air (< 10 s) upon mounting.

Thermogravimetry and Differential Scanning Calorimetry

Simultaneous Thermogravimetry (TGA) and Differential Scanning Calorimetry (DSC) measurements were performed with a Netzsch (STA 449 F3 Jupiter) under an argon flow of 40 mL·min^{-1} using Al crucibles containing approximately 7 mg of sample in a Pt furnace. The crucible lids were pierced ~10 seconds before being placed in the instrument. The analysis was conducted by heating from 40 – 300 °C at 10 °C·min^{-1}. $KB_{11}H_{14}$ was also analysed under heating and cooling (40 – 170 – 40 °C) at 10 °C·min^{-1}. The furnace containing the sample was evacuated prior to being placed under an argon flow.

Thermal Decomposition Analysis by Mass Spectrometry (TDA-MS)

Thermal decomposition data was obtained by Mass Spectrometry (MS) analysis of the evolved gas using a Stanford Research Systems (SRS) residual gas analyser (RGA-300) equipped with a quadrupole mass spectrometer. The samples (~5 mg) were placed inside a stainless steel reactor under an argon atmosphere, sealed, and heated from 25 to 300 °C (2 $°C \cdot min^{-1}$) under high vacuum ($< 8 \times 10^{-4}$ mbar). Temperature was controlled with a tube furnace and monitored by a K-type thermocouple ~5 mm from the sample.

Powder X-Ray Diffraction

Crystallographic phase analysis was performed at room temperature with X-Ray Powder Diffraction (XRPD) measurements by employing a Bruker D8 Advance Powder Diffractometer with a Cu K_α radiation source ($\lambda = 1.54056$ Å) run at 40 kV/40mA with a LynxEye detector in the 2θ range of 5 − 60°. The powder was mounted inside an argon glovebox on a single-crystal Si low background sample holder and sealed with an airtight poly(methyl-methacrylate) (PMMA) dome.

Additionally, XRPD data of the $NaB_{11}H_{14}{\cdot}(H_2O)_n$ sample were collected on a ThermoFisher ARL Equinox 5000 diffractometer using a Mo source (Mo K_α radiation, $\lambda = 0.7093$ Å) at room temperature and at −100 °C. The powdered sample was mounted inside an argon glovebox and sealed within a borosilicate capillary (OD 0.7 mm). The sample was cooled under a constant stream of liquid nitrogen, and the temperature was monitored by a K-type thermocouple ~10 mm from the capillary. Data were acquired using a curved position sensitive X-ray detector (CPS 120) with acquisition in real time over 120° 2θ.

Synchrotron Powder X-Ray Diffraction

Synchrotron XRPD data were collected at the powder diffraction beamline at the Australian Synchrotron using a wavelength of $\lambda = 0.563476(5)$ Å, which was refined using a NIST LaB_6 660b line position standard. $KB_{11}H_{14}$ powder was loaded into 0.7 mm borosilicate capillary and sealed with a flame. Data were collected on a Mythen II microstrip detector at two positions, and later combined into gap-free data sets, from 1° – 76° 2θ. A data set was collected at both 20 °C and 177 °C after collecting data for 240 s and 460 s, respectively. Additionally, *in-situ* XRPD data were collected during heating and cooling, where the sample was heated from 20 °C to 177 °C at 5 °C/min and then cooled at 6 °C/min to room temperature. Temperature was controlled using an Oxford Cryosystems Cryostream Plus.

Crystallographic indexing and structure solution were performed using Bruker Topas. The room temperature $KB_{11}H_{14}$ structure was solved using simulated annealing, treating the $B_{11}H_{14}^-$ units as rigid bodies. The structure was then refined with the Rietveld method. A minor impurity of K_2SO_4 was also modelled during structure solution. The background was defined using an 11th order Chebyshev polynomial. Unit cell parameters, scale factors, zero-point, peak shape mixing parameters and occupancies of K and B atoms were refined together. Isotropic displacement parameters, B_{iso}, were refined as a single parameter for the K and B atoms, while those for H were not refined. The supplementary crystallographic data has been deposited into the Inorganic Crystal Structure Database (CSD 2090015).

Single-Crystal X-Ray Crystallography

A single crystal of $LiB_{11}H_{14}{\cdot}2H_2O$ was grown by allowing an aliquot of the diethyl ether layer (obtained during synthesis after performing the liquid-liquid extraction step) to dry naturally at room temperature inside an argon filled glovebox. The crystal was mounted inside a glovebox, where it was transferred to a borosilicate capillary and sealed. The capillary containing the clear light colourless block-shaped crystal with dimensions $0.24 \times 0.18 \times 0.14$ mm^3 was then mounted onto a XtaLAB Synergy-S diffractometer, with data collected at 294.9(3) K. Data were measured using ⍰-scans using Cu K_α radiation. The diffraction pattern was indexed and the total number of runs and images was based on the strategy calculation from the program CrysAlisPro (Rigaku, V1.171.40.53, 2019).[1] The maximum resolution that was achieved was $\theta = 67.894°$ (0.83 Å). The unit cell was refined using CrysAlisPro (Rigaku, V1.171.40.53, 2019)[1] on 3182 reflections.

Data reduction, scaling, and absorption corrections were performed using CrysAlisPro (Rigaku, V1.171.40.53, 2019).[1] The final completeness was 66.30 %, which was low, as the sample became dislodged inside the capillary during data collection and could not be recovered. Numerous (~22) other 'single-crystal' samples were screened, however all were highly polycrystalline, making structure solution impossible. A multi-scan absorption correction was performed using CrysAlisPro 1.171.40.53 (Rigaku Oxford Diffraction, 2019).[1] The absorption coefficient μ of this material is 0.388 mm^{-1} at this wavelength (λ = 1.54184Å) and the minimum and maximum transmissions are 0.154 and 1.000.

The structure was solved and the space group *C*2/*c* (# 15) determined by the ShelXT[2,3] structure solution program using dual methods and refined by full matrix least squares minimisation on F^2 using version 2018/3 of ShelXL.[2–4] All non-hydrogen atoms were refined anisotropically. Hydrogen atom positions on the water ligands, and on the $B_{11}H_{14}^-$ cage were found in a difference map, then refined freely with 1,2 and 1,3-restraints used to optimize their geometry. The supplementary crystallographic data has been deposited into the Inorganic Crystal Structure Database (CSD 2031335).

Electrochemical Evaluation

Electrochemical Impedance Spectroscopy (EIS) was performed on pellets using a ZIVE SP1 electrochemical workstation. The powdered samples were pressed into pellets (6 mm diameter, ~1 mm thickness) under an argon atmosphere at 200 MPa, sandwiched between gold foil (0.1 mm thickness), and sealed within an air tight 'Swagelok-type' Teflon cell with 316 stainless steel electrodes. Temperature was monitored by a K-type thermocouple ~5 mm from the pellet and controlled with a tube furnace from room temperature to 100 °C, for $LiB_{11}H_{14}\cdot(H_2O)_n$ and $NaB_{11}H_{14}\cdot(H_2O)_n$, and to 160 °C for $KB_{11}H_{14}$ samples. The cells of $LiB_{11}H_{14}\cdot(H_2O)_n$ and $NaB_{11}H_{14}\cdot(H_2O)_n$ were also cooled down to 0 °C using an ice bath, −20 °C using a bath of ice and sodium chloride, as well as both −30 °C and −40 °C using a bath of dry ice and acetonitrile. EIS was conducted at 100 mV AC from 100 Hz to 1 MHz after 30 minutes of thermal equilibrium at each temperature. Ion conductivity data (σ) were derived from Nyquist impedance plots as:

$$\sigma = \frac{d}{l \times A} \quad (1)$$

where σ is the conductivity value in $S\cdot cm^{-1}$, *d* is the pellet thickness in cm, *A* is the area of the pellet face in cm^2 and *l* is the *x*-intercept of the Nyquist blocking tail. This tail accounts for the diffusion of ions in the electrolyte.[5] The uncertainty on each ion conductivity data point (± 10 %) is based on the *x*-intercept of the Nyquist plot and has little impact on the logarithmic-scale, where ion conductivities span many orders of magnitude. Ionic conductivity measurements of all samples were also performed after ball-milling them individually. Each powder was ball-milled inside an Across International Planetary Ball Mill (PQ-N04) with a ball-to-powder mass ratio of 10:1 employing stainless steel vials and balls (6 mm in diameter) under an argon atmosphere for 12 hour at a speed of 400 rpm.

Linear sweep voltammetry (LSV) was performed to investigate the oxidative stability of $LiB_{11}H_{14}\cdot(H_2O)_n$, $NaB_{11}H_{14}\cdot(H_2O)_n$ and $LiBH_4$ based on a method proposed by Han et. al.[6] and Asakura et. al.[7] $LiBH_4$ was used as a control sample to compare the results with previously published papers.[7,8] The material to be tested was mixed with graphite, previously heated to 550 °C under vacuum for 12 h, in a weight ratio of 75:25 by grinding 5 times with a mortar and pestle. Graphite is added in order to improve the contact area between electrolyte and current collector, to enhance the decomposition kinetics by increasing the electronic conductivity of the solid electrolyte, and to simulate a bulk-type all-solid-state-battery, where the electrode is formed by a mixture of carbon, solid electrolyte and active material.[6,7] 3 mg of the mixture was layered on top of 40 mg of the pristine material, which were pressed together at 200 MPa under argon to form a two layered pellet. This pellet was sandwiched to form a Al/Pt/sample+C/sample/(Li or Na) configuration, which was sealed within an air tight 'Swagelok-type' Teflon cell. LSV was conducted at 60 °C with a scan rate of 50 $\mu V\cdot s^{-1}$ from 1.5 V to 8.0 V for the *nido*-boranes, and from 1.5 to 4.5 V for $LiBH_4$. A second LSV cycle was also applied for the *nido*-boranes from 1.5 to 4.5 V at the same scan rate and temperature. The oxidative stability of the material was determined from the intersection point of two linear lines with $R^2 > 0.99$ (the background and the oxidative current).[7]

Temperature Programmed Photographic Analysis (TPPA)

A pellet of $KB_{11}H_{14}$ (~ 50 mg) on top of a gold foil was pressed at 200 MPa, transferred to a glass tube under an argon atmosphere and placed in a custom-made brass heating block. The sample was heated from RT to 170 °C ($\Delta T/\Delta t$ = 10 °C/min) while photos of the sample were collected every five seconds.[9]

Theoretical Calculations

All geometry optimisations and vibrational frequency calculations were carried out using Gaussian 09.[10] All methods were used as implemented. The geometry optimisation and vibrational frequency calculations were fully optimised on a B31LYP/aug-cc-pvdz level of theory (Table S1-4).[11] Molecules were drawn and evaluated using Diamond v3.2 and rendered using POVRAY (Fig. S22). Charges were calculated via the Natural Bond Orbital (NBO) analyses (Table S5).[12] NMR single-point calculations were carried out using the gauge-including atomic orbital (GIAO)-based approach[13] in acetonitrile using the conductor like polarisable continuum model (CPCM) as the solvation model (Table S6-7).[14] It has been shown that the inclusion of the implicit solvent model in the NMR calculation step is crucial to improve the prediction accuracy of calculated chemical shifts.[15] All ^{11}B chemical shifts are relative to the computed shielding of $BF_3O(C_2H_5)_2$ as the reference compound with an additional correction of +1.83.[16]

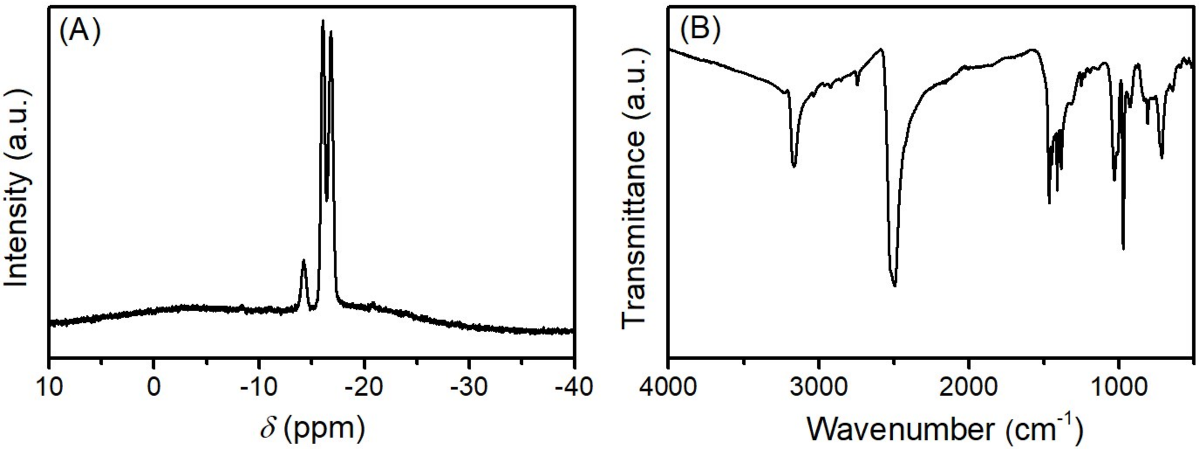

Figure S1. Spectroscopic characterization of $(CH_3)_3NHB_{11}H_{14}$. (A) $^{11}B\{^1H\}$ NMR spectrum (128 MHz) in CD_3CN. δ ($B_{11}H_{14}^-$) = −14.2, −16.0 and −16.8 ppm (B) FTIR spectrum with stretching modes at 3165 (^+N-H), 2495 (B−H), and 970 cm^{-1} ($C-N^+$), and bending modes at 1466 (CH_3), 1448 (CH_3), 1385 (CH_3), 1413 (^+N-H) and 1032 cm^{-1} (B−H).[17]

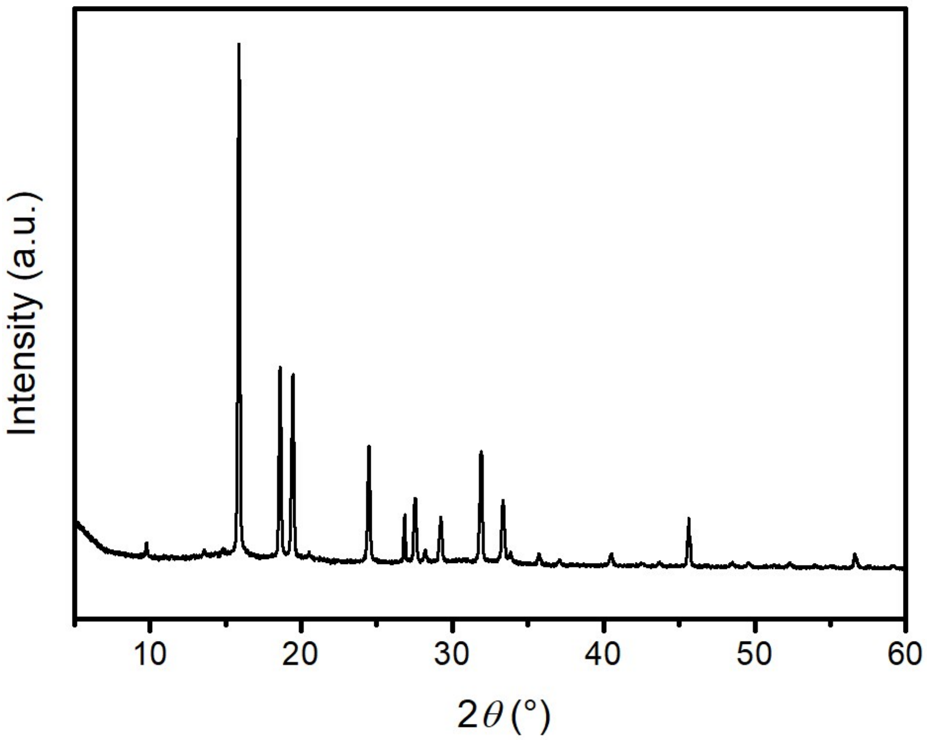

Figure S2. XRPD pattern ($\lambda_{\mathrm{Cuk}\alpha}$ = 1.54056 Å) for $(CH_3)_3NHB_{11}H_{14}$ at room temperature.

An aliquot of the aqueous solution obtained from the reaction of $(CH_3)_3NHB_{11}H_{14}$ with LiOH was dissolved in D_2O and analysed through ^{11}B NMR (Figure S3). $B_{11}H_{13}^{2-}$ is represented by the signals at −20.6 and −31.7 ppm.[18] Additional resonances are also observed from $B(OH)_4^-$ at 1.62 ppm[19] and BH_4^- at −41.9 ppm,[20] which are expected to be formed in boron based aqueous solutions with high pH.

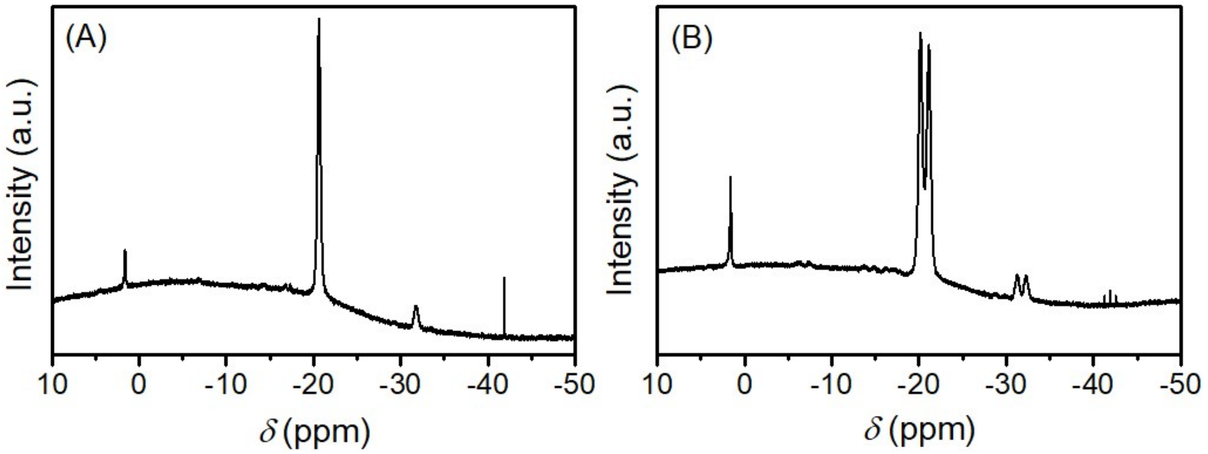

Figure S3. (A) $^{11}B\{^1H\}$ and (B) ^{11}B NMR spectra (D_2O, 128 MHz) of aqueous solution resulting from the reaction of $(CH_3)_3NHB_{11}H_{14}$ with LiOH after heating.

Figure S4 compares the $^{11}B\{^1H\}$ NMR spectra of the aqueous solution of the reaction of $(CH_3)_3NHB_{11}H_{14}$ with LiOH at different pH, adjusted with addition of HCl 1 mol·L^{-1} aqueous solution. $B_{11}H_{13}^{2-}$ (−20.6 ppm) is progressively converted into $B_{11}H_{14}^-$ (triplet at −15.1, −16.2 and −17.3 ppm) as the pH of the medium is reduced, and its resonance is no longer observed after reducing the pH below 5.0. Boric acid is also obtained as a side product of the reaction (δ = 19.4 ppm).

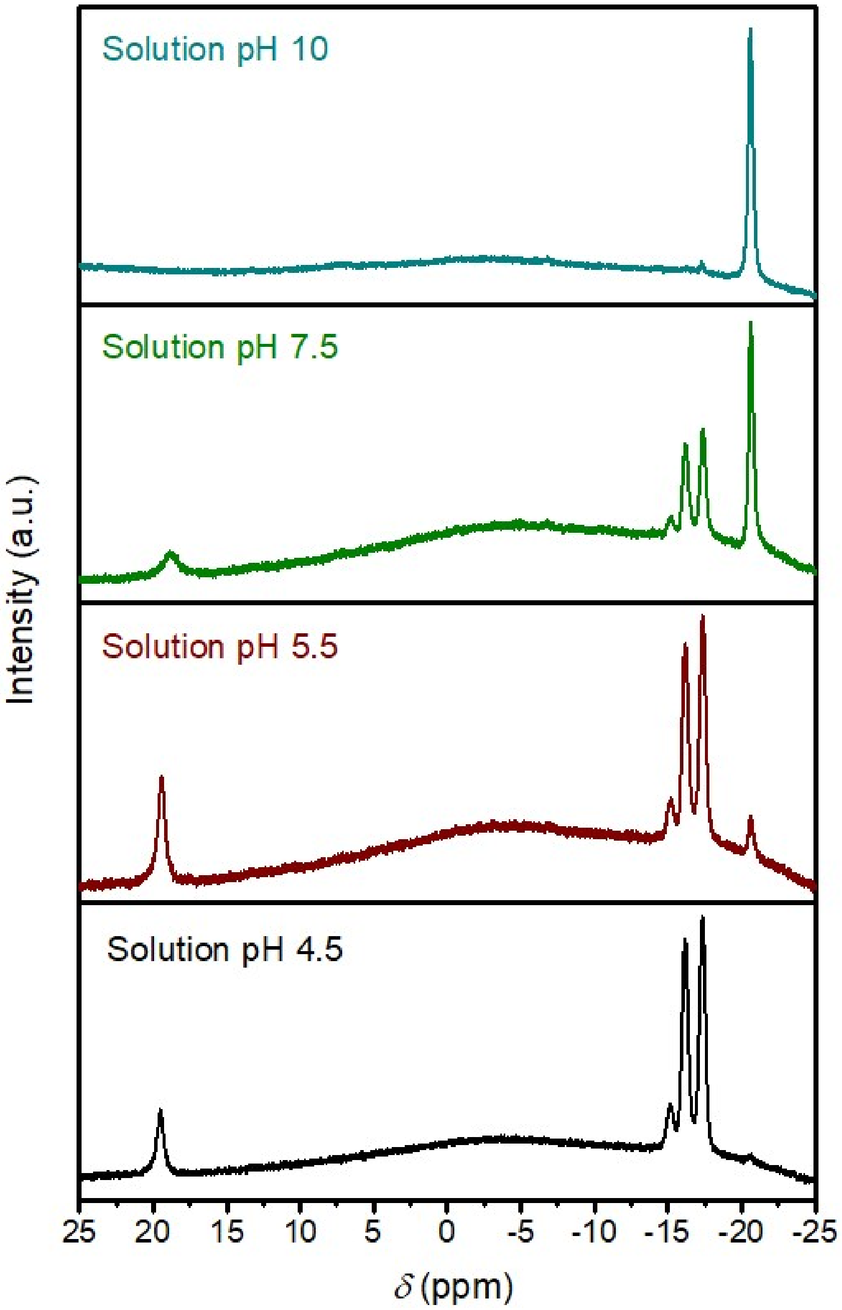

Figure S4. ^{11}B {^1H} NMR spectrum (128 MHz) in D_2O of aqueous solution of $Li_2B_{11}H_{13}$ after reducing its pH with addition of 1 mol·L^{-1} HCl solution to 10 (blue spectrum), 7.5 (green spectrum), 5.5 (red spectrum) and 4.5 (black spectrum).

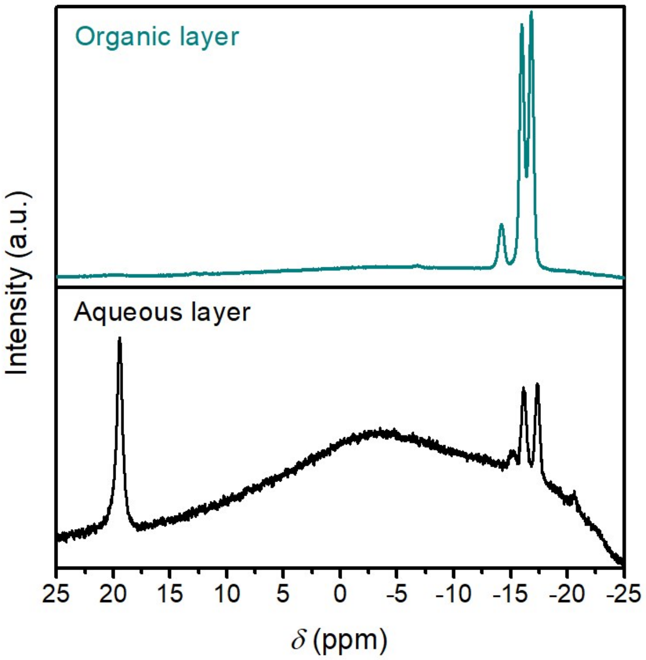

Figure S5. $^{11}B\{^1H\}$ NMR spectrum (128 MHz) of diethyl ether layer (top) in DMSO-d_6 after conducting a liquid-liquid extraction of the aqueous solution at pH 4.5, and $^{11}B\{^1H\}$ NMR spectrum (128 MHz) of the aqueous layer in D_2O after performing the extraction (bottom). The resonances at $\delta = -14.2, -16.0$ and -16.8 ppm in the top $^{11}B\{^1H\}$ NMR spectrum represent $B_{11}H_{14}^-$. Boric acid is observed at $\delta = 19.4$ ppm in the aqueous layer (bottom spectrum), and the small triplet represent remaining $B_{11}H_{14}^-$ that was not extracted by diethyl ether.

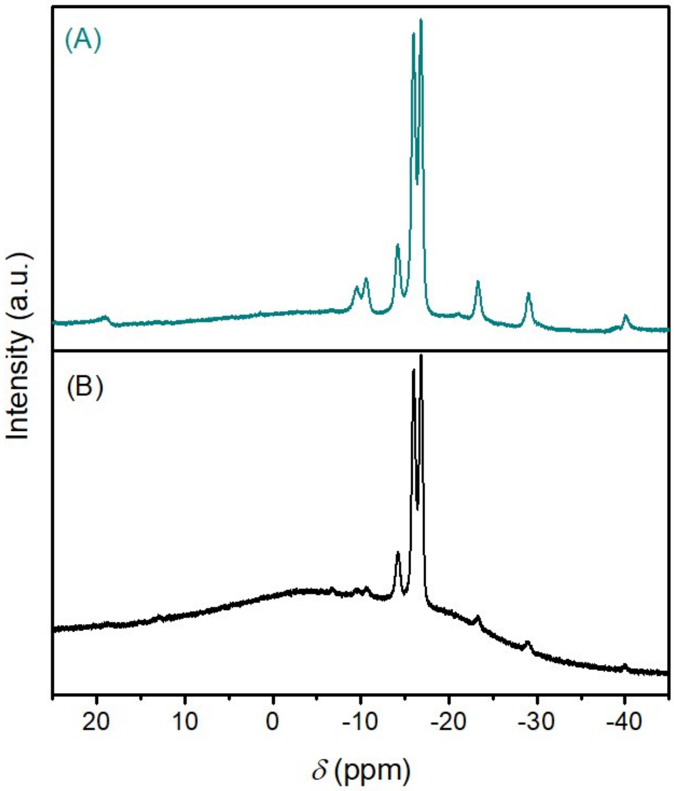

Figure S6. $^{11}B\{^1H\}$ NMR spectra (128 MHz) in DMSO-d_6 of $LiB_{11}H_{14}$ obtained after drying the organic layer that was extracted from aqueous solution at (A) pH 4.5 and (B) pH 7.5 at 80 °C. The amount of $B_{11}H_{13}OH^-$ is approximately 12 mol% in (A) and 4 mol% in (B) based on integration of the NMR peaks.

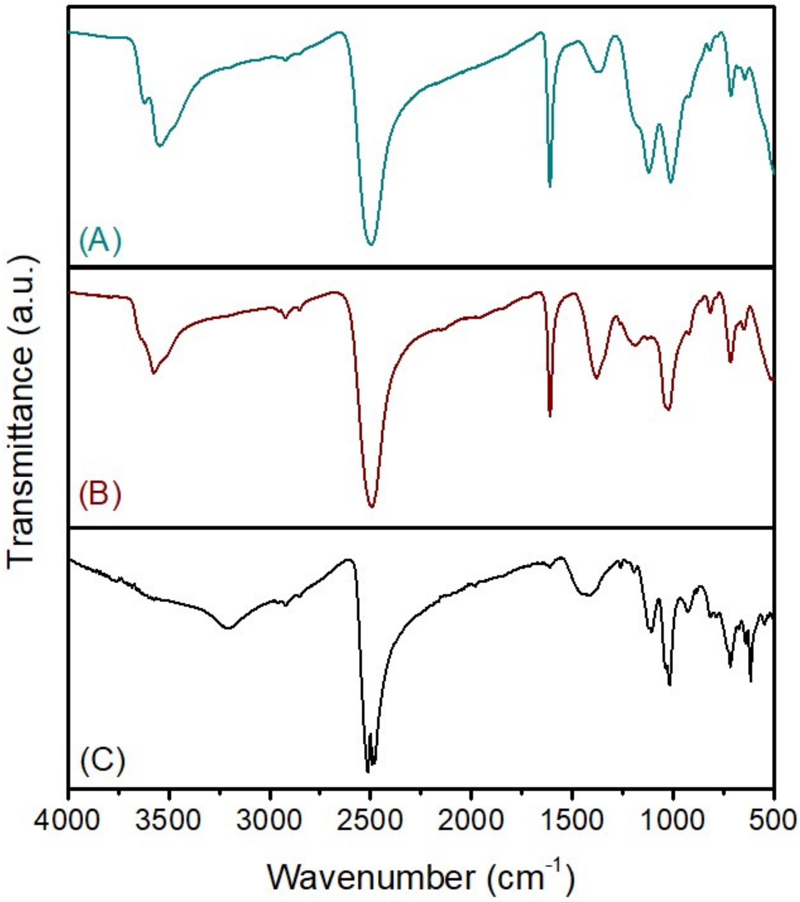

Figure S7. FTIR transmittance spectra of solid-state (A) $LiB_{11}H_{14}\cdot(H_2O)_n$, (B) $NaB_{11}H_{14}\cdot(H_2O)_n$, and (C) $KB_{11}H_{14}$. The wide band observed at 3200 - 3800 cm^{-1} (O−H stretching) and the sharp band at 1610 cm^{-1} (H−O−H bending) in (A) and (B) confirm the presence of water in the compounds.[21] The B−H stretching frequency is identified as a sharp peak at ~2500 cm^{-1} and the B−H bending mode is observed at ~1020 cm^{-1} for all the samples.[22]

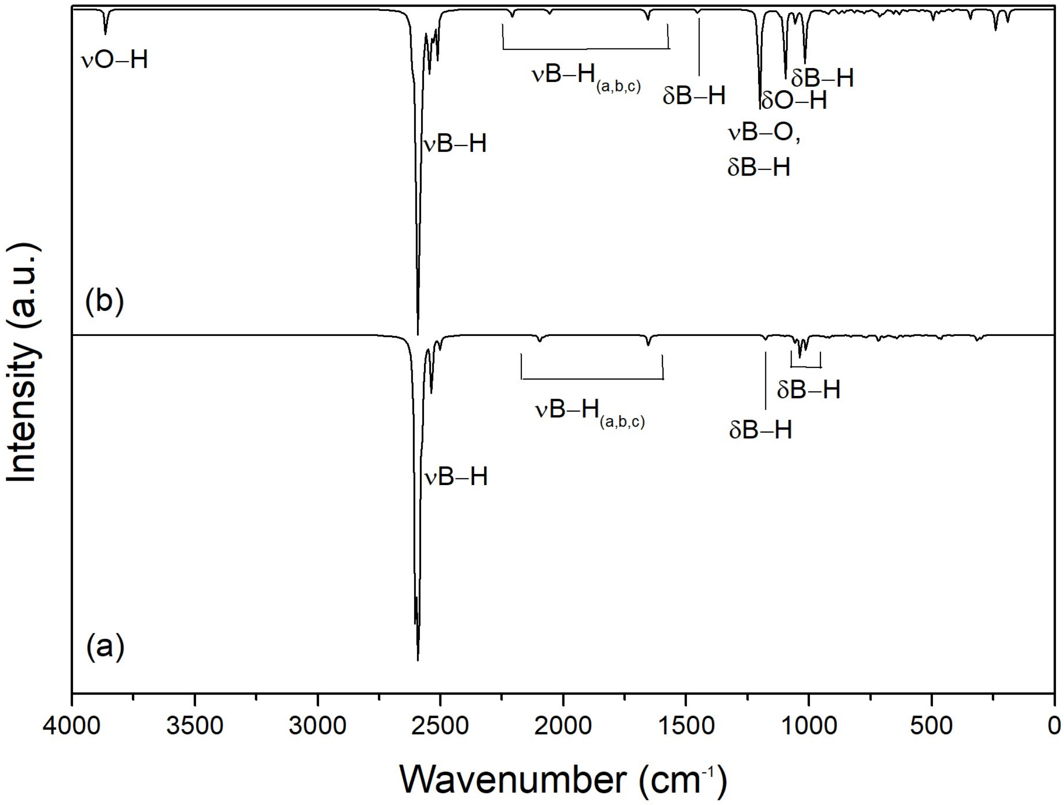

Figure S8. FTIR spectra of (a) $B_{11}H_{14}^-$ and (b) $B_{11}H_{13}OH^-$ calculated at the B31LYP/aug-cc-pvdz level of theory.

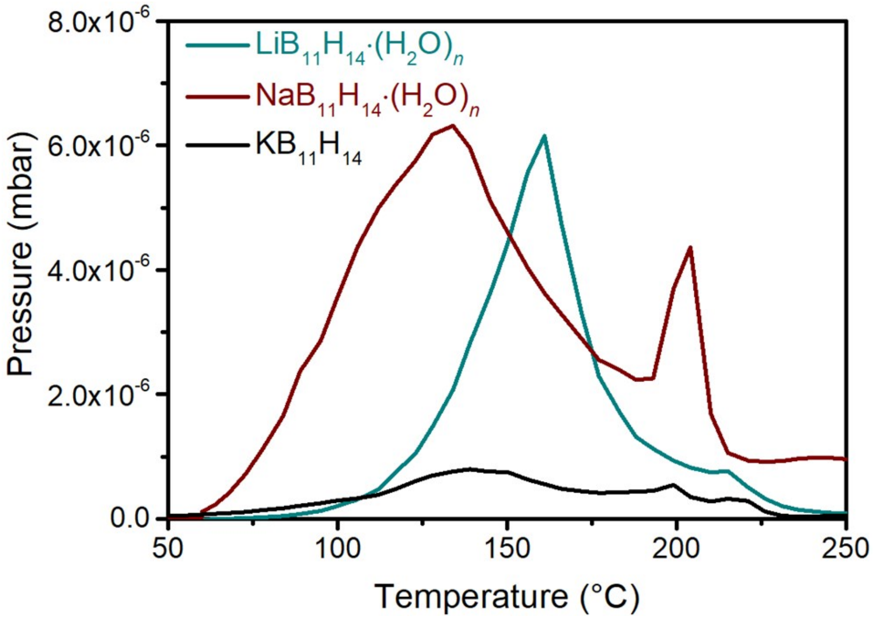

Figure S9. TDA-MS data at *m/z* 18 (water) of solid-state $LiB_{11}H_{14}\cdot(H_2O)_n$, $NaB_{11}H_{14}\cdot(H_2O)_n$, and $KB_{11}H_{14}$ samples. Approximately 5 mg of each compound was used for analysis and heated from 25 to 300 °C ($\Delta T/\Delta t$ = 2 °C·min^{-1}) under high vacuum (< 8 x 10^{-4} mbar).

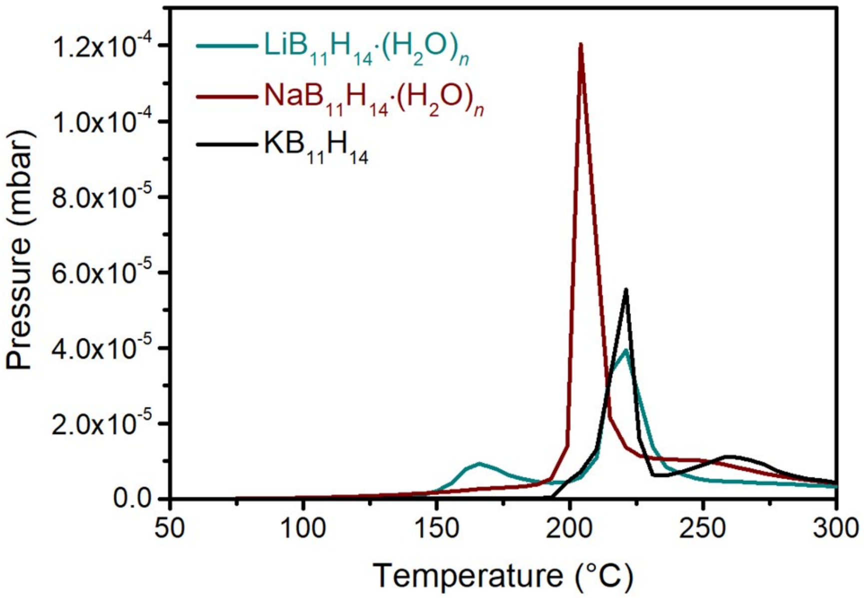

Figure S10. TDA-MS data at *m/z* 2 (hydrogen) of solid-state $LiB_{11}H_{14}\cdot(H_2O)_n$, $NaB_{11}H_{14}\cdot(H_2O)_n$, and $KB_{11}H_{14}$ samples. Approximately 5 mg of each compound was used for analysis and heated from 25 to 300 °C ($\Delta T/\Delta t$ = 2 °C·min^{-1}) under high vacuum (< 8 x 10^{-4} mbar).

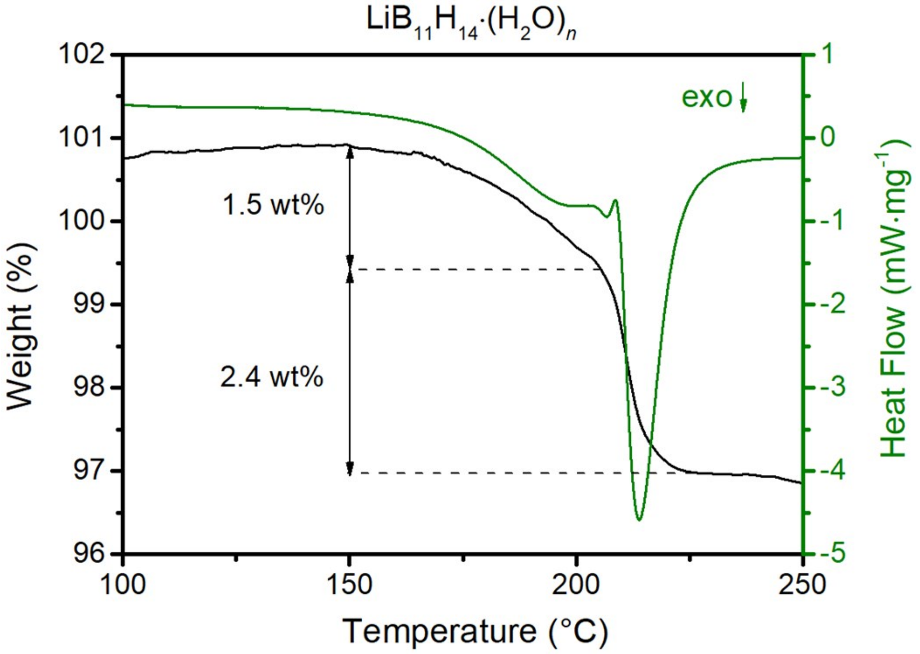

Figure S11. TGA-DSC measurement of $LiB_{11}H_{14}\cdot(H_2O)_n$ in the temperature range 100 – 250 °C ($\Delta T/\Delta t$ = 10 °C·min^{-1}, Ar flow = 40 mL·min^{-1}). Approximately 7 mg of compound was used for analysis. A mass loss of 1.5% is observed between 150 and 205 °C, which may be attributed to water and hydrogen release, and 2.4% between 205 and 225 °C from hydrogen release, as a result of decomposition of the material.

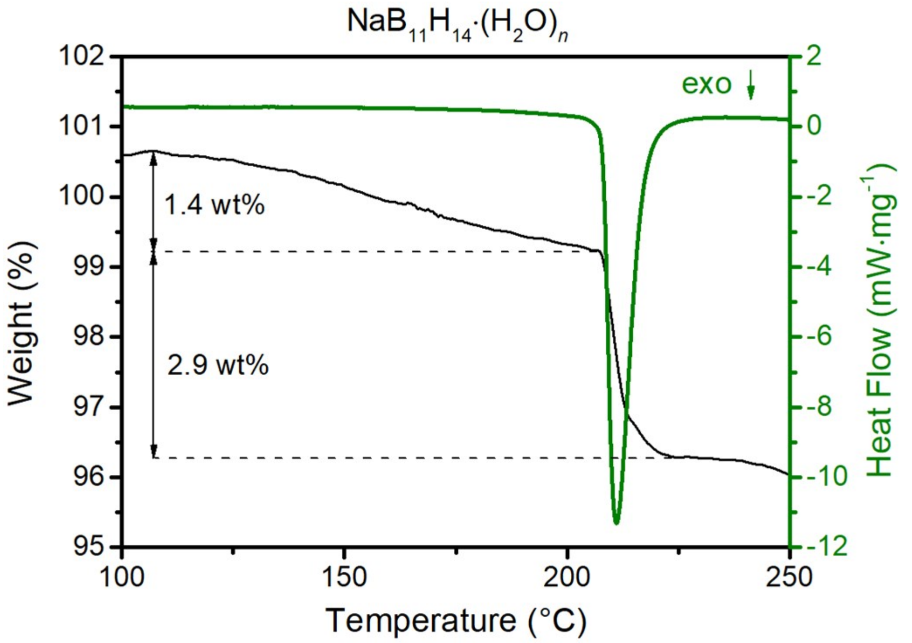

Figure S12. TGA-DSC measurement of $NaB_{11}H_{14}\cdot(H_2O)_n$ in the temperature range 100 – 250 °C ($\Delta T/\Delta t$ = 10 °C·min^{-1}, Ar flow = 40 mL·min^{-1}). Approximately 7 mg of compound was used for analysis. A mass loss of 1.4% is observed between 100 and 205 °C, which may be attributed to water release, and 2.9% between 205 and 225 °C from hydrogen and water release, as a result of decomposition of the material.

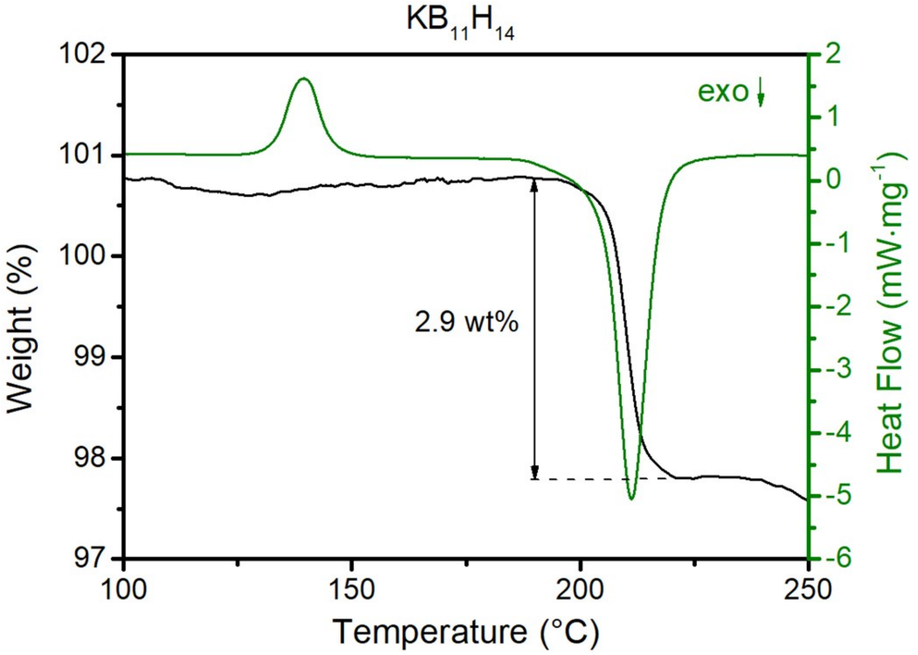

Figure S13. TGA-DSC measurement of $KB_{11}H_{14}$ in the temperature range 100 – 250 °C ($\Delta T/\Delta t$ = 10 °C·min^{-1}, Ar flow = 40 mL·min^{-1}). Approximately 7 mg of compound was used for analysis. The sample undergoes a phase transition at 140 °C represented by the endothermic peak on DSC plot and loses 2.9% of mass between 200 and 220 °C from hydrogen release, as a result of decomposition of the material.

Table S1. Structural Data Extracted from Refinements of the XRD Data for $KB_{11}H_{14}$ and $LiB_{11}H_{14}\cdot 2H_2O$

	α-$KB_{11}H_{14}$	$LiB_{11}H_{14}\cdot 2H_2O$
Mr	172.13	175.99
Space group	$P\bar{1}$	*C*2/*c*
T (°C)	25	21.9
Crystal System	Triclinic	Monoclinic
Colour/habit	-	colourless block
a (Å)	7.19499(8)	10.4298(4)
b (Å)	7.04622(8)	10.1040(2)
c (Å)	19.4087(2)	42.341(2)
α (°)	90.7188(7)	90
β (°)	94.0453(7)	91.236(4)
γ (°)	89.9709(7)	90
V (Å3)	981.44(1)	4461.0(3)
Z	2	16
ρ (g/cm3)	1.16949(2)	1.048

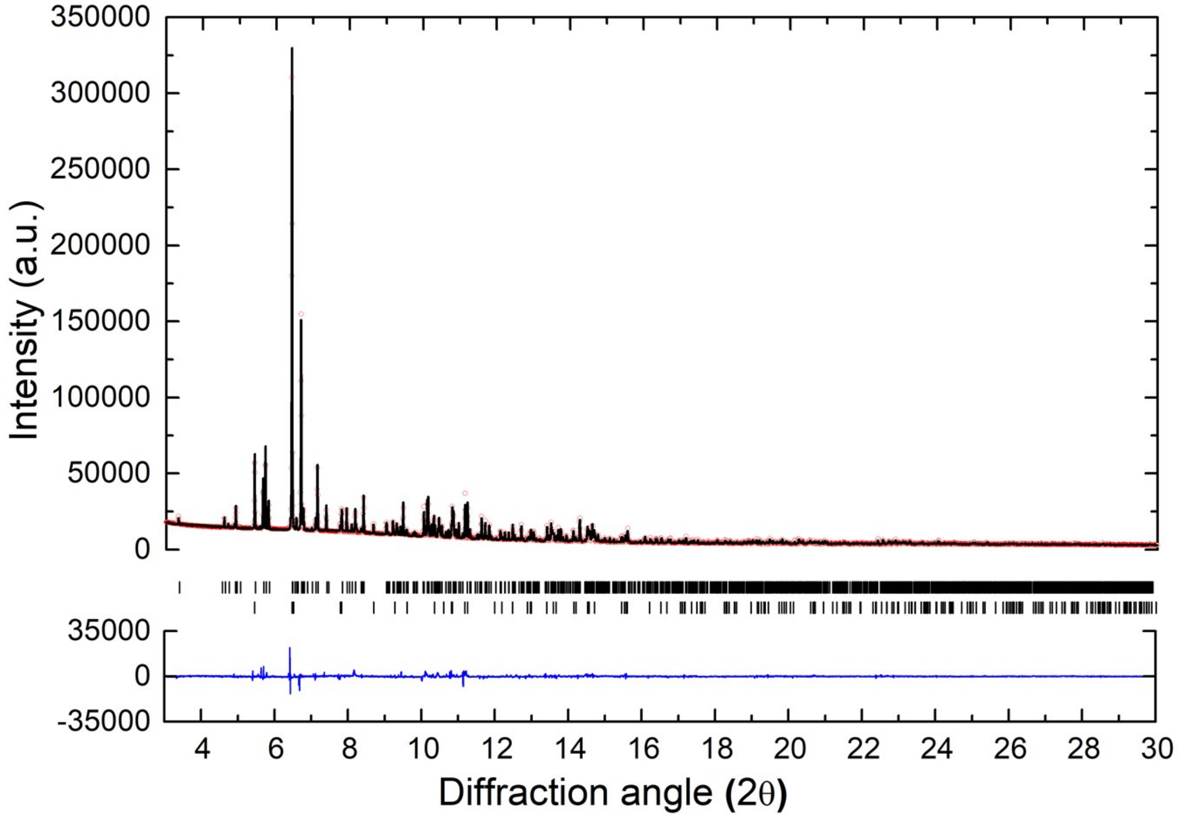

Figure S14: XRD data and Rietveld refinement plot for $KB_{11}H_{14}$. Experimental data as red circles, calculated diffraction pattern as black line and the difference plot in blue. Tick marks show positions (listed top to bottom) for (a) α-$KB_{11}H_{14}$ ($P\bar{1}$, 86.9(2) wt%); (b) K_2SO_4 (*Pnam*, 13.1(2) wt%). R_{wp} = 4.85. λ = 0.563476(5) Å.

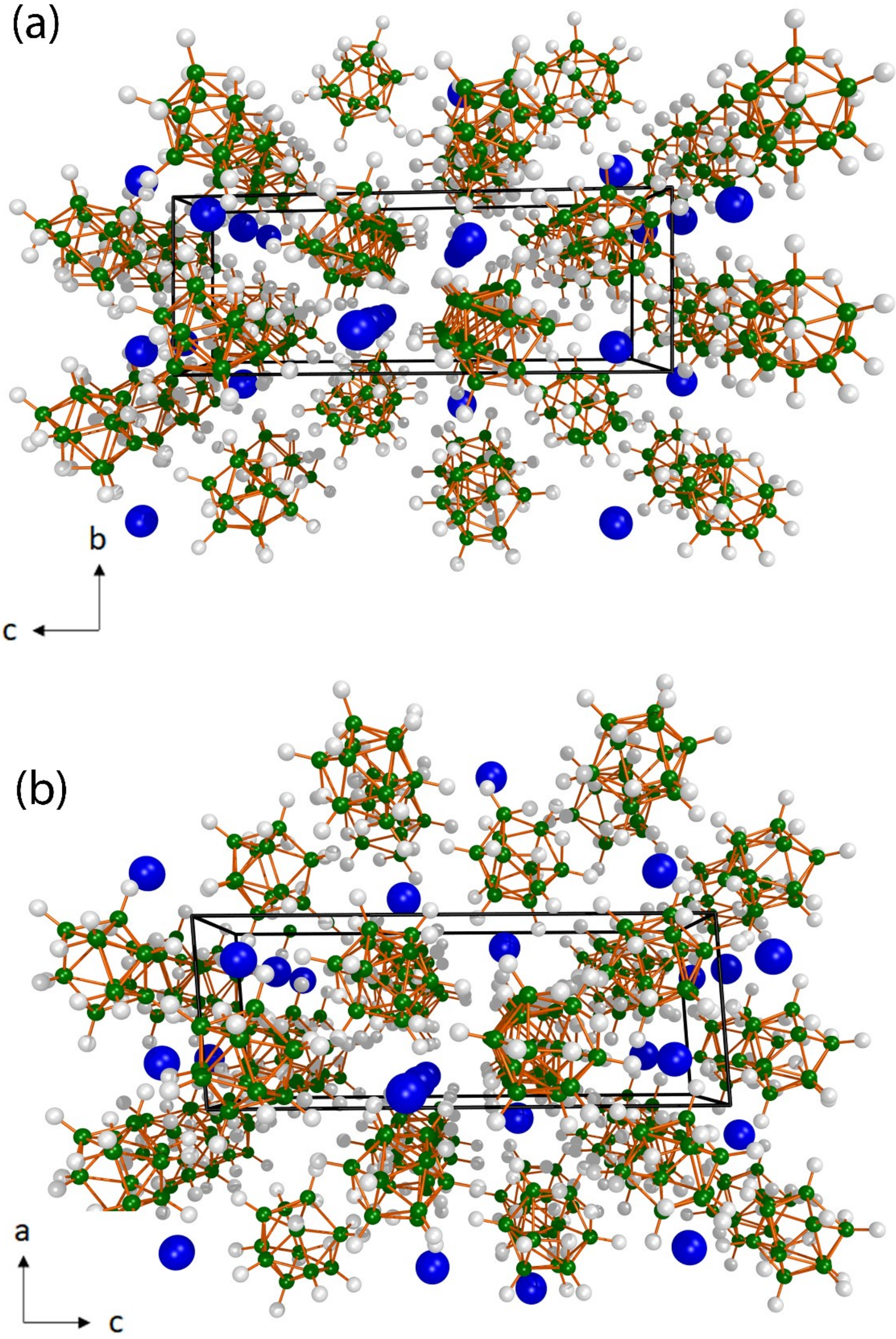

Figure S15: Crystal structure of α-$KB_{11}H_{14}$ ($P\bar{1}$). K (blue), B (green), H (white). Structure viewed (a) along the *a*-axis and (b) along the *b*-axis.

Table S2. The refined $KB_{11}H_{14}$ structural parameters at 25 °C in space group $P\bar{1}$ derived from PXRD data.

Atom	Wyck.	*x*/a	*y*/b	*z*/c	B_{iso} (Å^2)
K1	2i	0.8851(5)	0.2735(5)	0.6002(2)	5.00(8)
K2	2i	0.2382(5)	0.8775(5)	0.9081(2)	5.00(8)
B1a	2i	0.201(7)	0.893(5)	0.081(2)	2.91(9)
B2a	2i	0.224(6)	0.653(5)	0.056(2)	2.91(9)
B3a	2i	0.045(6)	0.725(5)	0.106(2)	2.91(9)
B4a	2i	0.420(7)	0.793(6)	0.076(2)	2.91(9)
B5a	2i	0.137(8)	0.898(6)	0.167(2)	2.91(9)
B6a	2i	0.367(8)	0.939(6)	0.149(2)	2.91(9)
B7a	2i	0.158(6)	0.510(5)	0.121(2)	2.91(9)
B8a	2i	0.411(6)	0.556(6)	0.102(2)	2.91(9)
B9a	2i	0.105(7)	0.669(6)	0.194(2)	2.91(9)
B10a	2i	0.501(7)	0.741(7)	0.162(2)	2.91(9)
B11a	2i	0.316(8)	0.822(7)	0.226(2)	2.91(9)
B1b	2i	0.777(5)	0.400(8)	0.419(2)	2.91(9)
B2b	2i	0.892(5)	0.320(7)	0.347(2)	2.91(9)
B3b	2i	0.692(4)	0.461(8)	0.336(2)	2.91(9)
B4b	2i	0.876(7)	0.176(7)	0.418(2)	2.91(9)
B5b	2i	0.534(5)	0.39(1)	0.397(2)	2.91(9)
B6b	2i	0.646(7)	0.211(9)	0.447(2)	2.91(9)
B7b	2i	0.729(5)	0.276(7)	0.279(2)	2.91(9)
B8b	2i	0.852(7)	0.083(7)	0.334(2)	2.91(9)
B9b	2i	0.497(5)	0.32(1)	0.312(2)	2.91(9)
B10b	2i	0.691(8)	0.015(9)	0.398(2)	2.91(9)
B11b	2i	0.454(7)	0.15(1)	0.388(2)	2.91(9)
H1a	2i	0.150(6)	0.007(5)	0.040(2)	3
H2a	2i	0.192(5)	−0.405(4)	−0.002(2)	3
H3a	2i	−0.107(6)	−0.267(4)	0.083(2)	3
H4a	2i	0.516(6)	−0.154(6)	0.034(2)	3
H5a	2i	0.048(7)	0.024(6)	0.188(2)	3

H6a	2i	0.426(7)	0.093(7)	0.158(3)	3
H7a	2i	0.090(4)	−0.640(4)	0.110(2)	3
H8a	2i	0.501(4)	−0.566(6)	0.079(2)	3
H9a	2i	0.001(6)	−0.370(6)	0.235(2)	3
H10a	2i	0.654(6)	−0.256(7)	0.183(3)	3
H11a	2i	0.332(8)	−0.073(7)	0.274(2)	3
H12a	2i	0.356(6)	−0.332(7)	0.246(2)	3
H13a	2i	0.206(5)	−0.487(6)	0.187(2)	3
H14a	2i	0.454(5)	−0.441(6)	0.167(2)	3
H1b	2i	0.844(5)	0.517(8)	0.456(2)	3
H2b	2i	1.041(5)	0.378(5)	0.332(1)	3
H3b	2i	0.702(4)	0.618(8)	0.321(2)	3
H4b	2i	1.004(7)	0.144(7)	0.456(2)	3
H5b	2i	0.430(5)	0.490(1)	0.422(2)	3
H6b	2i	0.613(7)	0.2(1)	0.505(2)	3
H7b	2i	0.764(4)	0.296(7)	0.221(2)	3
H8b	2i	0.960(7)	−0.018(6)	0.310(2)	3
H9b	2i	0.365(5)	0.36(1)	0.277(2)	3
H10b	2i	0.685(9)	−0.139(9)	0.418(2)	3
H11b	2i	0.317(7)	0.13(1)	0.417(3)	3
H12b	2i	0.443(7)	0.05(1)	0.339(2)	3
H13b	2i	0.576(6)	0.180(9)	0.276(2)	3
H14b	2i	0.697(7)	−0.009(8)	0.330(2)	3

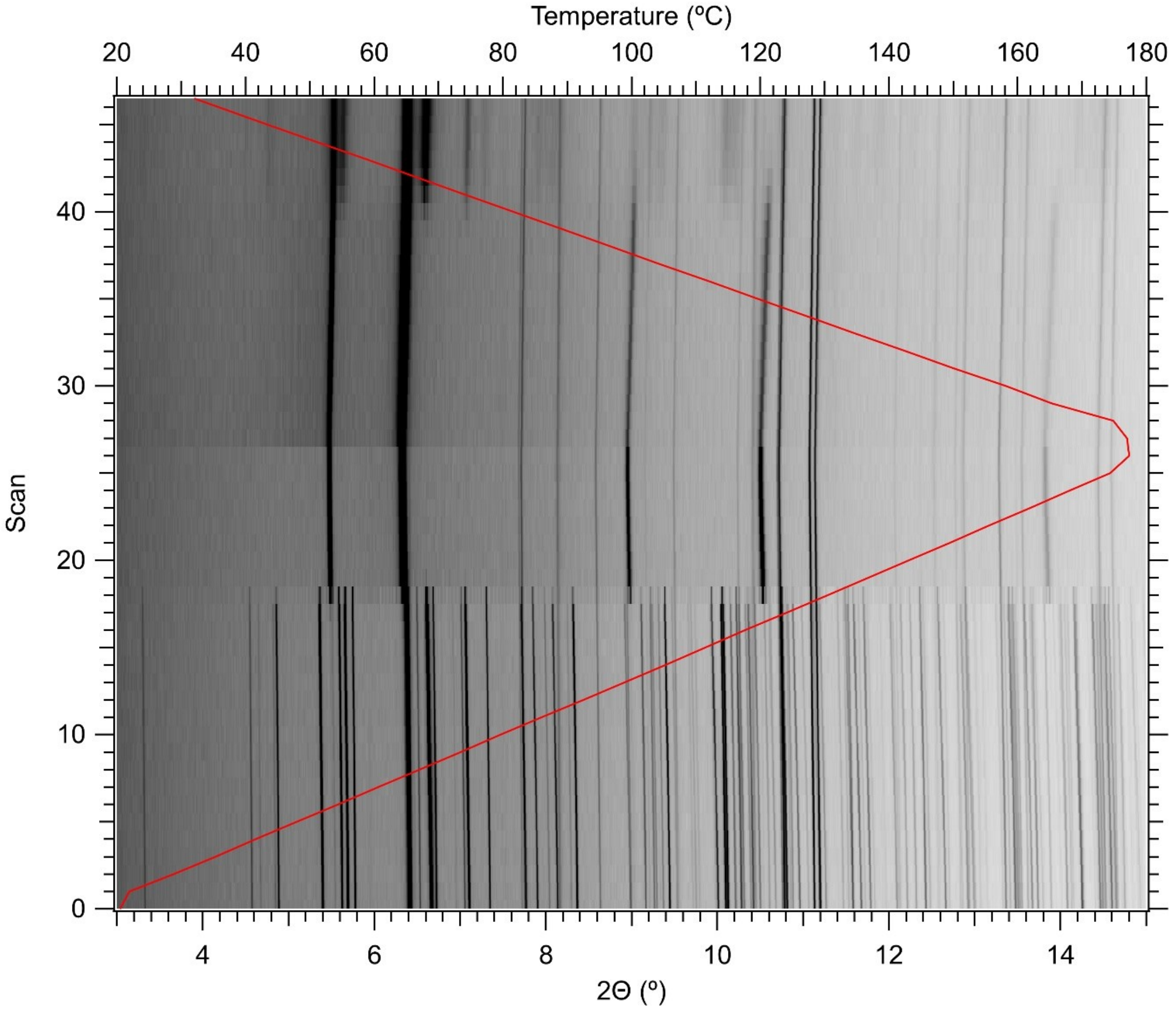

Figure S16. *In-situ* synchrotron PXRD data of $KB_{11}H_{14}$ during heating and cooling, λ = 0.563516(6) Å. A reversible polymorphic phase transition is seen near 135 °C on heating and 85 °C on subsequent cooling. A minor impurity of K_2SO_4 is present with persistent peaks across all temperatures (red line).

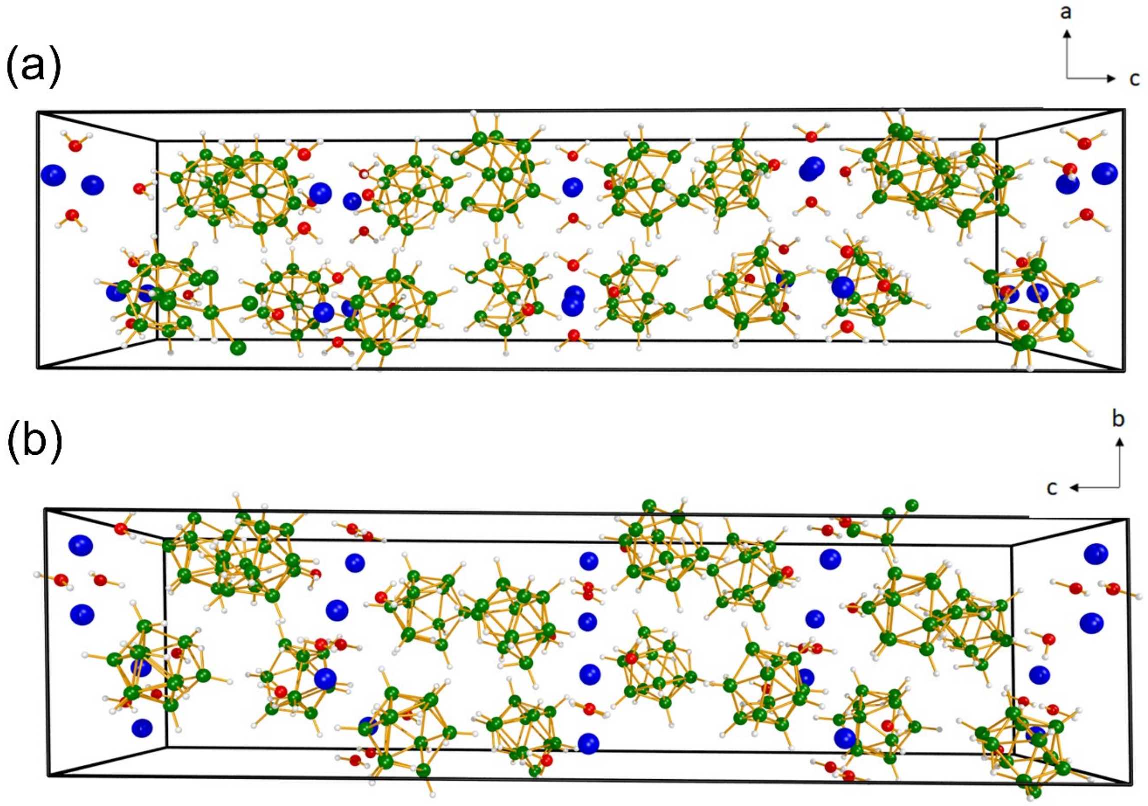

Figure S17: Crystal structure of $LiB_{11}H_{14}\cdot 2H_2O$ (*C*2/*c*). Li (blue), B (green), O (red) and H (white). The structure is viewed along the *b*-axis (top) and *a*-axis (bottom) demonstrating the lithium coordination that alternate along the *b*-axis.

Table S3: The refined $LiB_{11}H_{14}.2H_2O$ structural parameters at 21.9 °C in space group (*C*2/*c*) derived from single crystal data.

Atom	**Wyck.**	***x*/a**	***y*/b**	***z*/c**
O2	8f	0.4545(2)	0.7271(2)	0.54241(5)
H2B	8f	0.42117	0.68679	0.55859
H2C	8f	0.52588	0.76068	0.55007
O2A	8f	0.8125(2)	0.3153(2)	0.20068(6)
H2AA	8f	0.75406	0.26666	0.1911
H2AB	8f	0.84133	0.36618	0.18565
B5	8f	0.5663(4)	0.8048(4)	0.46150(7)
H5	8f	0.54815	0.84754	0.48487

B3A	8f	0.6705(4)	0.3418(4)	0.28396(7)
H3A	8f	0.67751	0.37254	0.25913
B3	8f	0.7491(4)	0.7261(4)	0.41607(7)
H3	8f	0.85034	0.71658	0.40968
B7	8f	0.4337(4)	0.7521(4)	0.43810(7)
B2A	8f	0.5407(4)	0.2437(4)	0.29710(7)
H2A	8f	0.46363	0.21069	0.28082
B1A	8f	0.6969(4)	0.1759(4)	0.29605(7)
H1A	8f	0.72186	0.09892	0.27887
B11A	8f	0.6500(4)	0.2352(4)	0.36123(7)
B6	8f	0.5425(4)	0.6338(4)	0.45308(7)
H6	8f	0.50835	0.56432	0.47104
B9	8f	0.6314(4)	0.6701(4)	0.38879(7)
B4	8f	0.6956(4)	0.8616(4)	0.43887(7)
H4	8f	0.76101	0.93936	0.44764
B1	8f	0.6990(4)	0.6992(4)	0.45494(7)
H1	8f	0.76684	0.67215	0.47412
B10	8f	0.6571(4)	0.8533(4)	0.39819(7)
B8	8f	0.4947(4)	0.6094(4)	0.41308(7)
B7A	8f	0.5025(4)	0.2813(4)	0.33670(8)
B4A	8f	0.8082(4)	0.2989(4)	0.30761(7)
H4A	8f	0.90541	0.30158	0.29804
B10A	8f	0.7877(4)	0.3402(4)	0.34743(7)

B5A	8f	0.7624(4)	0.1752(4)	0.33497(7)
H5A	8f	0.82941	0.09788	0.34321
B6A	8f	0.5983(4)	0.1415(4)	0.32833(8)
H6A	8f	0.55843	0.04208	0.33213
B9A	8f	0.7284(4)	0.4493(4)	0.31402(8)
B8A	8f	0.5511(4)	0.4134(4)	0.30712(7)
B11	8f	0.5352(4)	0.9019(4)	0.42742(8)
B2	8f	0.6569(4)	0.5848(4)	0.42515(8)
H2	8f	0.69741	0.4843	0.42499
Li1	8f	0.3882(5)	0.7388(5)	0.50118(13)
Li1A	8f	0.8648(7)	0.3113(5)	0.24386(16)
O1	8f	0.24039(17)	0.60442(16)	0.49970(4)
H1B	8f	0.20839	0.54534	0.51594
H1C	8f	0.25809	0.5614	0.48295
O1A	4e	1	0.1678(2)	0.25
O3A	4e	1	0.4543(2)	0.25
H8A	8f	0.482(2)	0.489(2)	0.2981(7)
H10A	8f	0.861(2)	0.369(3)	0.3649(7)
H9A	8f	0.772(3)	0.541(2)	0.3064(7)
H7AA	8f	0.404(2)	0.267(3)	0.3449(7)
H11A	8f	0.642(3)	0.199(3)	0.3854(5)
H10C	8f	0.703(3)	0.916(3)	0.3809(7)
H7A	8f	0.339(2)	0.766(3)	0.4476(7)
H8	8f	0.443(3)	0.518(2)	0.4087(7)

H9B	8f	0.658(3)	0.624(3)	0.3665(4)
H11	8f	0.503(3)	1.003(2)	0.4288(7)
H10D	8f	0.554(2)	0.878(3)	0.4026(5)
H10B	8f	0.737(3)	0.437(2)	0.3411(4)
H11B	8f	0.619(3)	0.3397(16)	0.3612(7)
H7AB	8f	0.525(3)	0.3877(14)	0.3317(4)
H9C	8f	0.5195(17)	0.671(3)	0.3905(5)
H7B	8f	0.421(3)	0.795(3)	0.4138(4)
H1AA	8f	1.013(4)	0.118(3)	0.2342(4)
H3AA	8f	1.017(3)	0.504(3)	0.2346(4)

The ionic conductivity results for all samples were determined from their Nyquist plots based on the intercept of the electrode spike on the real axis (Z'). Figure S18 shows the Nyquist plots for the pristine samples of $LiB_{11}H_{14}\cdot(H_2O)_n$ and $NaB_{11}H_{14}\cdot(H_2O)_n$ at some specific temperatures, and Figure S19 shows the Nyquist plots for the pristine and ball-milled (B.M.) samples of $KB_{11}H_{14}$ at 100 and 160 °C.

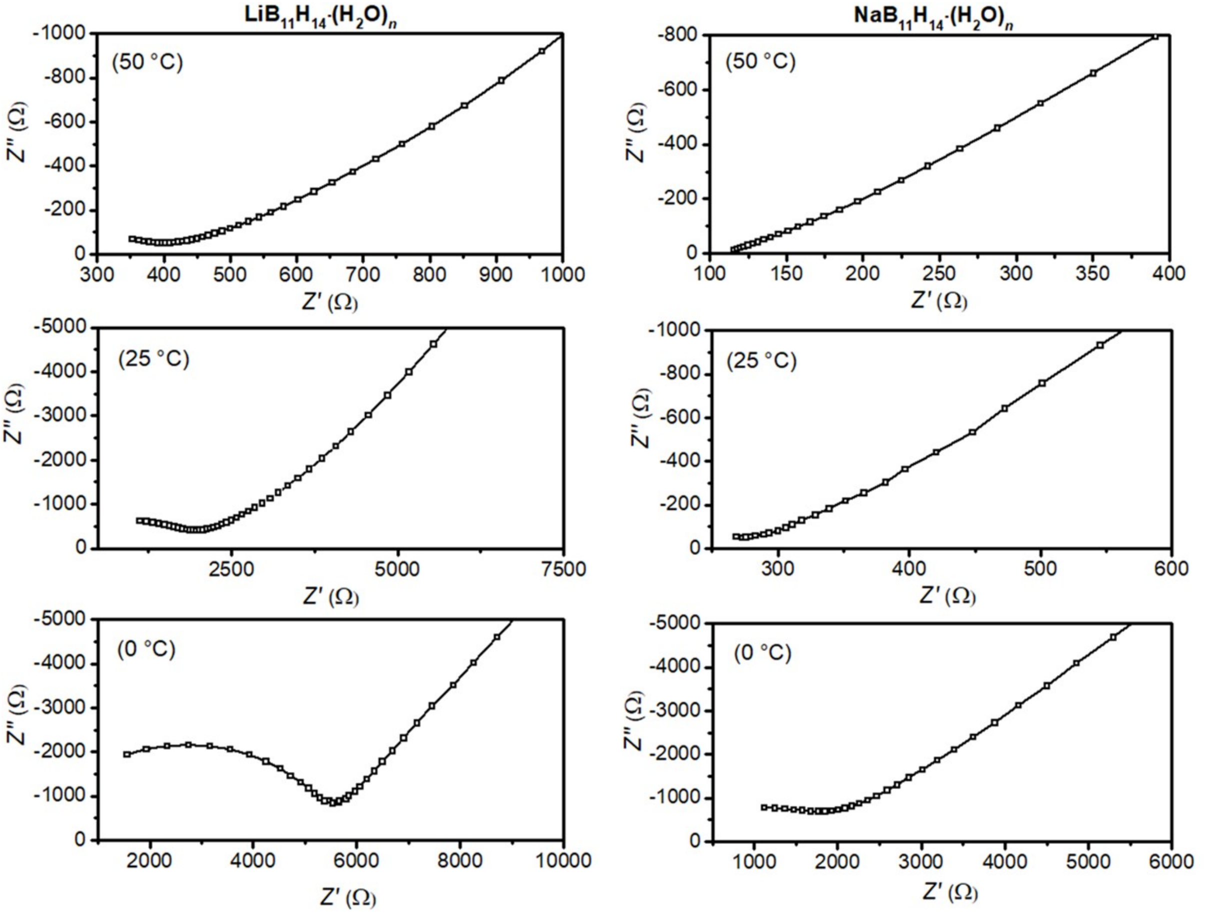

Figure S18. Magnified Nyquist plot of pristine $LiB_{11}H_{14}\cdot(H_2O)_n$ (left) and $NaB_{11}H_{14}\cdot(H_2O)_n$ (right) in the high-frequency region at 0, 25, and 50 °C.

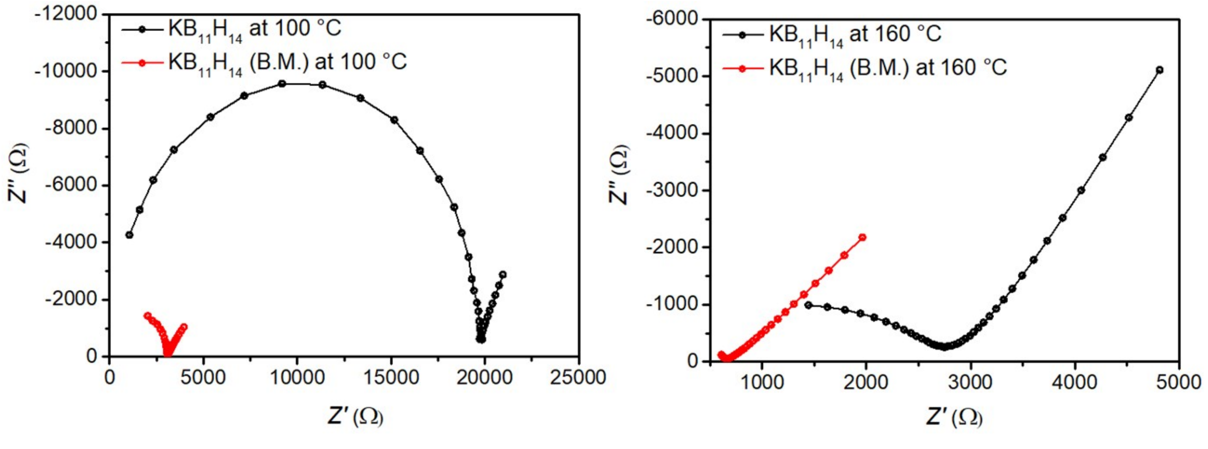

Figure S19. Nyquist plot of pristine and ball-milled (B.M.) $KB_{11}H_{14}$ at 100 °C (left) and 160 °C (right) from 100 Hz to 1 MHz.

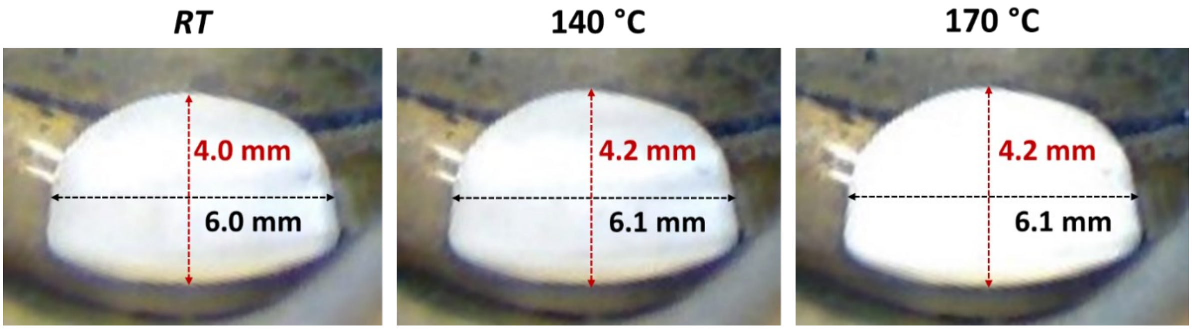

Figure S20. TPPA of $KB_{11}H_{14}$ heated from room temperature to 170 °C ($\Delta T/\Delta t$ = 10 °C·min^{-1}). A volume increase of the pellet can be observed at ~120-140 °C.

Full data set of the Arrhenius plot of ionic conductivity for the sample $KB_{11}H_{14}$ is presented in Figure S21. It is observed a drop in ionic conductivity at temperatures above 100 °C, which is related to the volume expansion of the pellet during its polymorphic structural transition, however it is an artefact. Ball-milled $KB_{11}H_{14}$ was run a second time, and the drop in ionic conductivity can still be observed, but with less intensity.

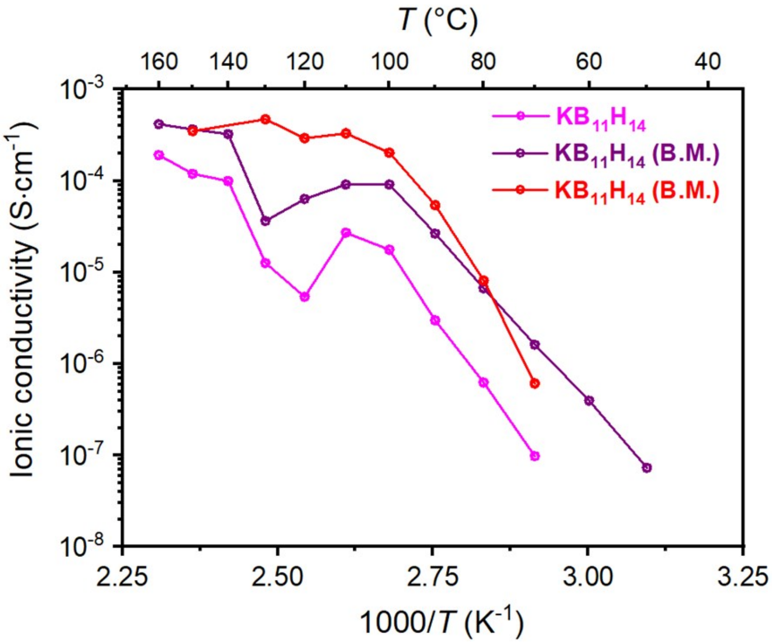

Figure S21. Ionic conductivity of pristine and ball-milled (two measurements) $KB_{11}H_{14}$ with data points between 110 and 130 °C. All measurements show a drop in ionic conductivity in this range of temperature, which is associated to the order-disorder phase transition.

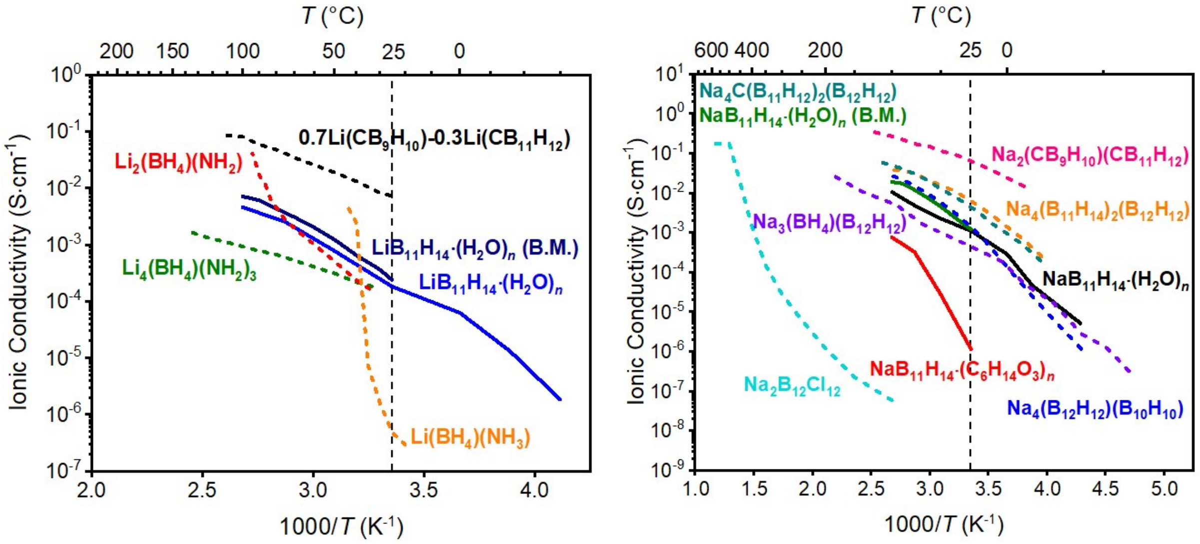

Figure S22. Arrhenius plots of ionic conductivities of $LiB_{11}H_{14}\cdot(H_2O)_n$, $NaB_{11}H_{14}\cdot(H_2O)_n$, and $NaB_{11}H_{14}\cdot(C_6H_{14}O_3)_n$ compared with other Li (left)[23–25] and Na (right)[5,26–30] mixed anion boron-hydrogen solid-state electrolytes. The solid lines represent the ionic conductivity of the materials synthesised in this work.

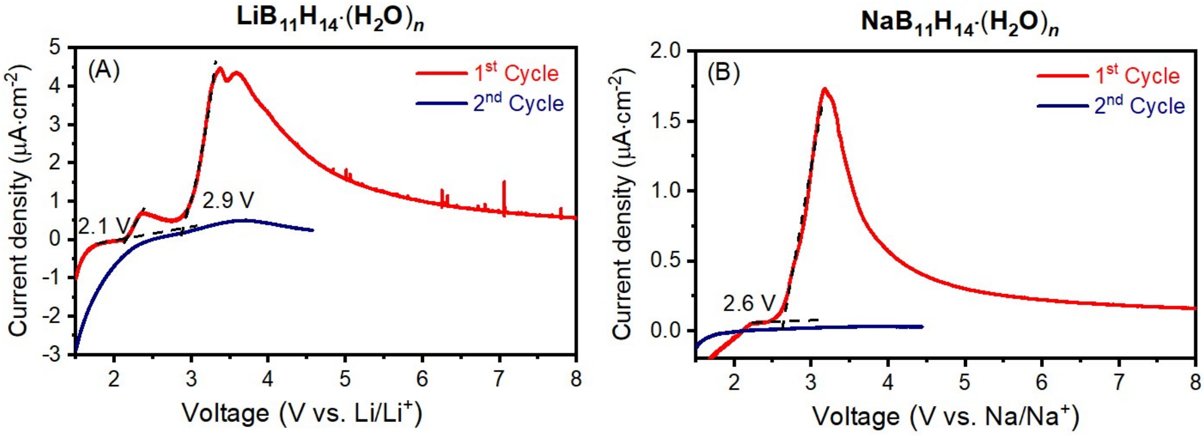

Figure S23. Linear Sweep Voltammograms of (A) $Li/LiB_{11}H_{14}\cdot(H_2O)_n/LiB_{11}H_{14}\cdot(H_2O)_n$+C/Pt/Al and (B) $Na/NaB_{11}H_{14}\cdot(H_2O)_n/NaB_{11}H_{14}\cdot(H_2O)_n$+C/Pt/Al cells at a scan rate of 50 μV·s^{-1} at 60 °C between 1.5 and 8.0 V (1st run) and 1.5 and 4.5 V (2nd run). The black dashed lines represent the linear regression lines fitted to the background and to the anodic current to obtain the oxidation potential.

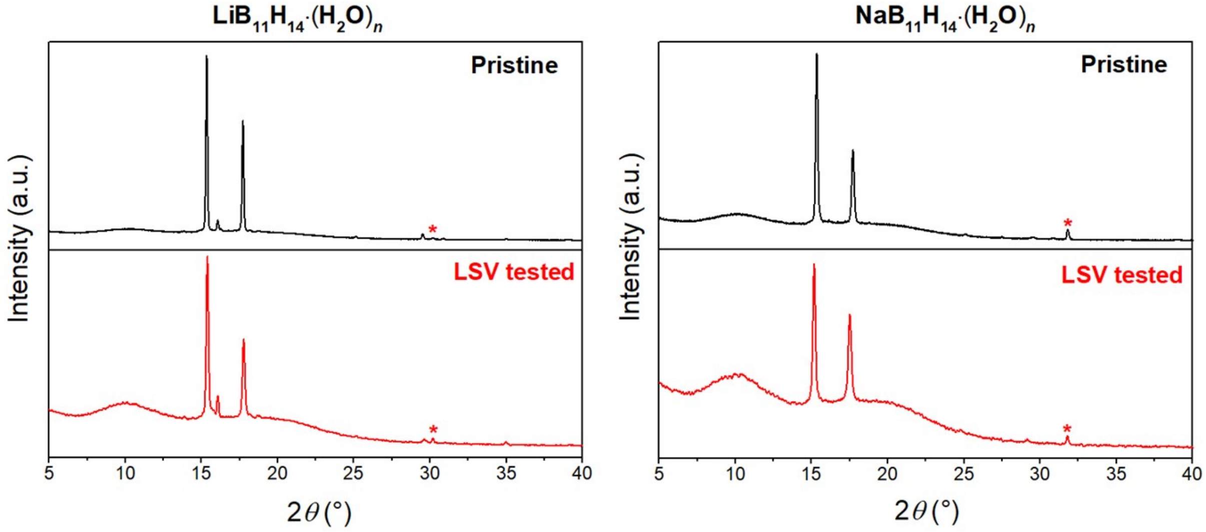

Figure S24. XRPD profiles of $LiB_{11}H_{14}\cdot(H_2O)_n$ (left) and $NaB_{11}H_{14}\cdot(H_2O)_n$ (right) at room temperature before (black) and after (red) second run of LSV experiment. Asterisks at 2θ = 30.2° in the $LiB_{11}H_{14}\cdot(H_2O)_n$ and at 31.8° in the $NaB_{11}H_{14}\cdot(H_2O)_n$ patterns represent inadvertent LiCl and NaCl contamination, respectively.

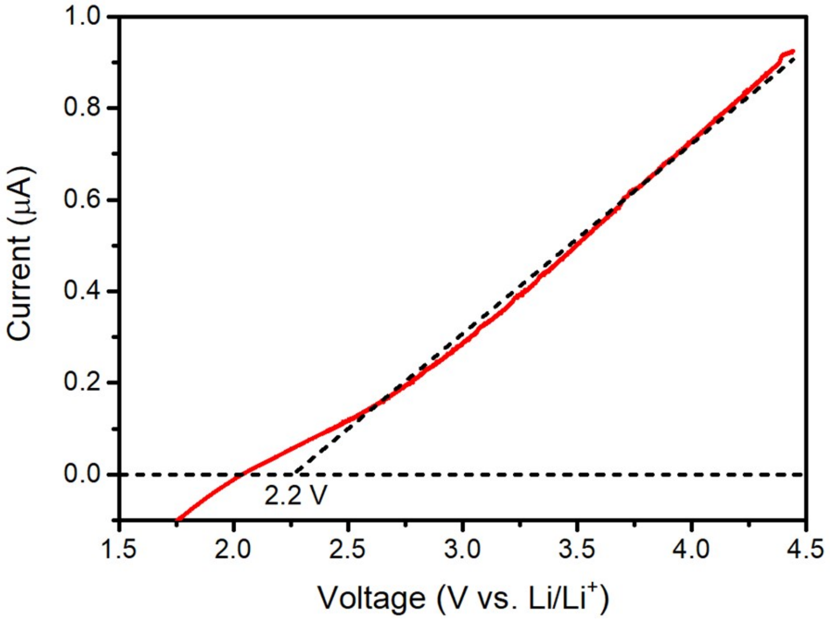

Figure S25. Linear Sweep Voltammogram of $Li/LiBH_4/LiBH_4$+C/Pt/Al cell at a scan rate of 50 $\mu V\cdot s^{-1}$ at 60 °C between 1.5 and 4.5 V. The black dashed lines represent the linear regression lines fitted to the background and to the anodic current to obtain the oxidation potential.

The result that was obtained for $LiBH_4$ (2.2 V) (Fig. S25) is close to the one previously detected using the same experimental method (2.04 V)[7] and from the one calculated by first principles computational methods (2.0 V).[8] This demonstrates the efficacy of the experiment to determine the oxidative stability limit of the *nido*-boranes investigated.

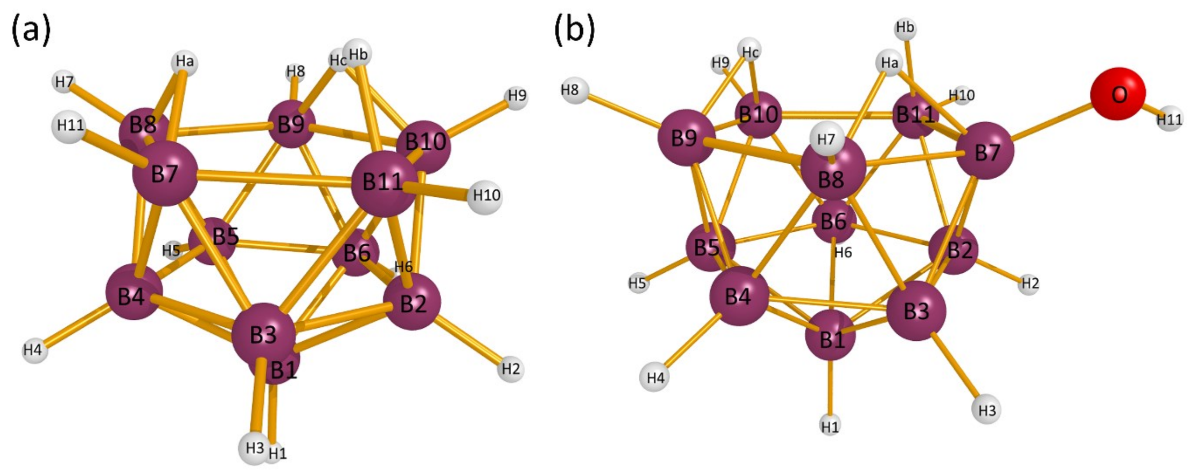

Figure S26. Calculated structure of (a) $B_{11}H_{14}^-$ and (b) $B_{11}H_{13}OH^-$. Boron atoms are violet spheres; H atoms are white spheres; O atom is red sphere.

DFT Calculations for $B_{11}H_{14}^-$ and $B_{11}H_{13}OH^-$

Table S4. Calculated bond distances and angles for $B_{11}H_{14}^-$ at B31LYP/aug-cc-pvdz level of theory.

Atoms	**Bond distance (Å)**	**Atoms**	**Bond Angles (°)**
B1 − B3	1.779	B1 − B2 − B10	110.49
B1 − B4	1.790	B1 − B2 − B11	111.17
B1 − H1	1.197	B1 − B2 − H2	121.16
B2 − B1	1.779	B1 − B3 − B11	111.17
B2 − B10	1.746	B1 − B3 − H3	121.15
B2 − B11	1.793	B1 − B4 − H4	119.98
B2 − B3	1.817	B1 − B5 − H5	125.56
B2 − H2	1.198	B1 − B6 − B10	108.03
B3 − H3	1.198	B1 − B6 − H6	119.98
B4 − B3	1.789	B2 − B1 − B4	110.01
B4 − H4	1.198	B2 − B1 − H1	121.15
B5 − B1	1.779	B2 − B10 − H9	125.04
B5 − B4	1.785	B2 − B10 − Hc	129.32
B5 − B6	1.785	B2 − B11 − H10	112.43
B5 − B8	1.760	B2 − B11 − Hb	128.77
B5 − B9	1.760	B2 − B3 − B4	108.36
B5 − H5	1.198	B2 − B3 − H3	120.57

B6 − B1	1.790	B2 − B6 − H6	122.31
B6 − B10	1.789	B3 − B1 − H1	121.15
B6 − B2	1.789	B3 − B11 − H10	112.42
B6 − H6	1.198	B3 − B11 − Hb	128.71
B7 − B3	1.746	B3 − B2 − B10	112.03
B7 − B4	1.789	B3 − B2 − H2	120.56
B7 − B8	1.860	B3 − B4 − H4	122.30
B7 − H11	1.196	B3 − B7 − H11	125.03
B7 − Ha	1.354	B3 − B7 − Ha	129.34
B8 − B4	1.778	B4 − B1 − H1	120.20
B8 − H7	1.199	B4 − B3 − B11	116.45
B8 − Ha	1.285	B4 − B3 − H3	121.51
B9 − B10	1.860	B4 − B5 − H5	120.68
B9 − B6	1.778	B4 − B7 − H11	125.74
B9 − H8	1.199	B4 − B7 − Ha	101.41
B9 − Hc	1.285	B4 − B8 − H7	123.04
B10 − H9	1.197	B4 − B8 − Ha	104.94
B10 − Hc	1.354	B5 − B1 − B2	106.64
B11 − B3	1.793	B5 − B1 − B3	106.64
B11 − H10	1.204	B5 − B1 − H1	123.56
B11 − Hb	1.211	B5 − B4 − B3	105.95
		B5 − B4 − H4	122.54
		B5 − B6 − B10	108.60
		B5 − B6 − B2	105.95
		B5 − B6 − H6	122.54
		B5 − B8 − H7	122.84
		B5 − B8 − Ha	130.40
		B5 − B9 − B10	106.58
		B5 − B9 − H8	122.85
		B5 − B9 − Hc	130.38
		B6 − B1 − B3	110.01

		B6 − B1 − B4	110.65
		B6 − B1 − H1	120.20
		B6 − B10 − H9	125.74
		B6 − B10 − Hc	101.42
		B6 − B2 − B11	116.45
		B6 − B2 − B3	108.37
		B6 − B2 − H2	121.52
		B6 − B5 − B4	111.09
		B6 − B5 − H5	120.69
		B6 − B9 − H8	123.05
		B6 − B9 − Hc	104.94
		B7 − B3 − B1	110.48
		B7 − B3 − B11	68.15
		B7 − B3 − B2	112.03
		B7 − B3 − H3	119.17
		B7 − B4 − B1	108.03
		B7 − B4 − B5	108.60
		B7 − B4 − H4	121.95
		B7 − B8 − B5	106.58
		B7 − B8 − H7	123.09
		B8 − B4 − B1	108.46
		B8 − B4 − B3	108.06
		B8 − B4 − H4	122.22
		B8 − B5 − B1	109.79
		B8 − B5 − B6	114.66
		B8 − B5 − B9	67.33
		B8 − B5 − H5	114.93
		B8 − B7 − B3	106.35
		B8 − B7 − H11	122.52
		B9 − B10 − B2	106.35
		B9 − B10 − H9	122.51

		B9 − B5 − B1	109.79
		B9 − B5 − B4	114.66
		B9 − B5 − H5	114.94
		B9 − B6 − B1	108.46
		B9 − B6 − B2	108.05
		B9 − B6 − H6	122.23
		B10 − B2 − H2	119.17
		B10 − B6 − H6	121.95
		B10 − B9 − H8	123.09
		B11 − B2 − B10	68.16
		B11 − B2 − H2	115.02
		B11 − B3 − H3	115.03
		H8 − B9 − Hc	105.06
		H11 − B7 − Ha	104.23
		Ha − B8 − H7	105.06
		Hb − B11 − H10	107.19
		Hc − B10 − H9	104.24

Table S5. Calculated bond distances and angles for $B_{11}H_{13}OH^{-}$ at B31LYP/aug-cc-pvdz level of theory.

Atoms	**Bond distance (Å)**	**Atoms**	**Bond Angles (°)**
B1 − B2	1.784	B1 − B2 − B11	110.92
B1 − B3	1.776	B1 − B2 − B7	110.76
B1 − B4	1.778	B1 − B2 − H2	120.56
B1 − B5	1.793	B1 − B3 − B7	109.03
B1 − B6	1.781	B1 − B3 − B8	109.22
B1 − H2	1.197	B1 − B3 − H3	120.79
B2 − B11	1.805	B1 − B4 − B8	109.75
B2 − B3	1.795	B1 − B4 − B9	109.74
B2 − B6	1.813	B1 − B4 − H4	125.78
B2 − B7	1.749	B1 − B5 − B10	108.51
B2 − H2	1.202	B1 − B5 − B9	108.18

B3 − B4	1.776	B1 − B5 − H5	119.51
B3 − B7	1.794	B1 − B6 − B10	110.67
B3 − B8	1.781	B1 − B6 − B11	112.23
B3 − H3	1.198	B1 − B6 − H6	120.78
B4 − B5	1.783	B2 − B1 − B4	106.48
B4 − B8	1.768	B2 − B1 − B5	109.79
B4 − B9	1.760	B2 − B11 − H10	111.86
B4 − H4	1.198	B2 − B11 − Hb	124.65
B5 − B10	1.778	B2 − B3 − B4	106.10
B5 − B6	1.791	B2 − B3 − B8	107.55
B5 − B9	1.780	B2 − B3 − H3	121.93
B5 − H5	1.198	B2 − B6 − B10	112.89
B6 − B10	1.743	B2 − B6 − B5	108.57
B6 − B11	1.781	B2 − B6 − H6	120.13
B6 − H6	1.198	B2 − B7 − B8	105.98
B7 − B8	1.863	B2 − B7 − Ha	126.22
B7 − Ha	1.404	B2 − B7 − O	127.25
B7 − Hb		B3 − B1 − B5	110.77
B7 − O	1.409	B3 − B1 − B6	110.27
B8 − H7	1.198	B3 − B2 − B11	117.34
B8 − Ha	1.266	B3 − B2 − B6	107.96
B9 − B10	1.856	B3 − B2 − H2	120.53
B9 − B11	1.294	B3 − B4 − B5	111.23
B9 − H8	1.198	B3 − B4 − B9	114.79
B10 − H2	1.197	B3 − B4 − H4	120.14
B10 − Hc	1.341	B3 − B7 − Ha	100.01
B11 − H10	1.206	B3 − B7 − O	127.87
B11 − Hb	1.207	B3 − B8 − H7	122.18
O − H11	0.962	B3 − B8 − Ha	106.65
		B4 − B1 − B6	106.42
		B4 − B3 − B7	109.43

		B4 − B3 − H3	123.80
		B4 − B5 − B10	109.20
		B4 − B5 − B6	105.74
		B4 − B5 − H5	122.13
		B4 − B8 − B7	106.71
		B4 − B8 − H7	122.11
		B4 − B8 − Ha	129.36
		B4 − B9 − B10	106.77
		B4 − B9 − H8	122.72
		B4 − B9 − Hc	130.73
		B5 − B10 − H9	125.34
		B5 − B10 − Hc	102.17
		B5 − B4 − B8	115.21
		B5 − B4 − H4	120.98
		B5 − B6 − B11	116.83
		B5 − B6 − H6	121.63
		B5 − B9 − H8	123.45
		B5 − B9 − Hc	104.12
		B6 − B10 − B9	106.17
		B6 − B10 − H9	125.38
		B6 − B10 − Hc	128.31
		B6 − B11 − H10	112.07
		B6 − B11 − Hb	132.50
		B6 − B2 − B7	113.62
		B6 − B2 − H2	121.15
		B6 − B5 − B9	107.40
		B6 − B5 − H5	122.66
		B7 − B2 − B11	70.37
		B7 − B2 − H2	117.98
		B7 − B3 − H3	119.45
		B7 − B8 − H7	122.71

		B8 − B3 − H3	121.72
		B8 − B4 − B9	67.56
		B8 − B4 − H4	114.25
		B8 − B7 − O	121.98
		B9 − B10 − H9	122.69
		B9 − B4 − H4	115.22
		B9 − B5 − H5	122.84
		B10 − B5 − H5	121.86
		B10 − B6 − H6	118.96
		B10 − B9 − H8	122.81
		B11 − B2 − H2	115.82
		B11 − B6 − B10	68.69
		B11 − B6 − H6	114.32
		H1 − B1 − B2	121.19
		H1 − B1 − B3	120.00
		H1 − B1 − B4	123.89
		H1 − B1 − B5	120.23
		H1 − B1 − B6	121.09
		H7 − B8 − Ha	106.44
		H10 − B11 − Hb	107.71
		Hc − B10 − H9	104.58
		Hc − B9 − H8	105.05
		O − B7 − Ha	104.66

Table S6. Optimised atomic coordinates for $B_{11}H_{14}^-$ at B31LYP/aug-cc-pvdz level of theory**.**

B	−1.56331	0.50444	−0.80203
B	0.00038	−1.5354	0.54625
B	−0.97547	−1.25756	−0.89188
B	0.97591	−1.25703	−0.89199
B	1.47225	−0.53083	0.65324
B	0.90827	1.16649	0.67459

B	0.00012	−0.07742	1.56505
B	−1.47191	−0.53146	0.6534
B	−0.00038	1.72421	−0.76662
B	−0.90867	1.16616	0.67474
B	1.56312	0.50505	−0.80215
H	−2.56885	0.87492	−1.33412
H	−0.96679	−0.28229	−1.72861
H	0.00056	−2.66496	0.94604
H	−1.59608	−2.12762	−1.43427
H	1.59679	−2.12671	−1.43471
H	0.9664	−0.28149	−1.72855
H	2.45399	−0.8867	1.24023
H	1.51707	2.02123	1.2516
H	0.00015	−0.10643	2.76199
H	−2.45346	−0.88772	1.24048
H	−0.00132	1.26493	−1.8868
H	−0.00067	2.92321	−0.8737
H	−1.5178	2.02055	1.25193
H	2.56846	0.87582	−1.33442

Table S7. Optimised atomic coordinates for $B_{11}H_{13}OH^-$ at B31LYP/aug-cc-pvdz level of theory.

B	0.86891	−0.09122	1.51075
H	1.2593	−0.12378	2.64195
B	−0.61776	0.79208	1.07138
B	−0.58295	−1.00238	1.0458
B	0.99884	−1.45481	0.37785
B	2.03862	−0.02353	0.15401
B	1.00678	1.3905	0.53285
B	−1.49924	−0.05975	−0.17546
B	−0.417	1.64758	−0.50521
H	−1.25005	1.37849	1.90832

B	−0.43541	−1.51269	−0.65441
H	−1.17865	−1.65912	1.85104
B	1.31452	−0.8513	−1.24517
H	1.47123	−2.52769	0.62433
B	1.35599	1.00029	−1.12934
H	3.21336	−0.04703	0.38614
H	1.46336	2.39361	1.00112
O	−2.89074	−0.04974	−0.3941
H	0.74982	0.09968	−1.91714
H	−0.81622	2.78425	−0.45327
H	−0.73708	1.19458	−1.57769
H	−0.89219	−2.54607	−1.05217
H	−0.95801	−0.59677	−1.35477
H	1.95268	−1.46586	−2.05186
H	1.98977	1.68099	−1.88238
H	−3.2978	0.65874	0.11389

Table S8. NPA charge and ^{11}B NMR spectroscopy chemical shift (ppm) analysis for $B_{11}H_{14}^-$ and $B_{11}H_{13}OH^-$ calculated at the B31LYP/aug-cc-pvdz level of theory.

Atom	**NPA Charge**		**Mulliken Charge**	
	$B_{11}H_{14}^-$	$B_{11}H_{13}OH^-$	$B_{11}H_{14}^-$	$B_{11}H_{13}OH^-$
B1	−0.130	−0.123	−1.853	−1.910
B2	−0.203	−0.270	−1.078	−1.494
B3	−0.203	−0.214	−1.080	−1.908
B4	−0.189	−0.192	−1.587	−0.460
B5	−0.192	−0.201	−0.376	−1.566
B6	−0.189	−0.206	−1.587	−0.975
B7	0.000	0.613	−2.554	1.132
B8	−0.147	−0.192	−2.835	−3.290
B9	−0.147	−0.122	−2.835	−2.878
B10	0.000	−0.022	−2.555	−2.674
B11	−0.308	−0.303	−2.800	−2.961

H1	0.032	0.032	1.484	1.517
H2	0.039	0.038	1.479	1.467
H3	0.039	0.037	1.479	1.492
H4	0.032	0.046	1.453	1.488
H5	0.044	0.034	1.431	1.423
H6	0.032	0.041	1.453	1.474
H7	0.025	0.032	1.639	1.634
H8	0.025	0.023	1.639	1.678
H9	0.010	0.013	1.653	1.659
H10	0.039	0.034	1.608	1.607
H11	0.010	0.495	1.653	0.185
Ha	0.127	0.117	1.115	1.080
Hb	0.124	0.101	0.936	0.955
Hc	0.127	0.128	1.115	1.134
O	–	−0.938	–	−0.812

Table S9. Observed and calculated ^{11}B NMR chemical shifts (ppm) for $B_{11}H_{14}^{-}$ calculated at the B31LYP/aug-cc-pvdz level of theory. Solvent is CD_3CN.

Atoms	$B_{11}H_{14}^{-}$	
	Observed	Calculated
B1	−14.2	−10.9
B2−6	−16.8	−18.4
B7−11	−16.0	−13.2

Table S10. Observed and calculated ^{11}B NMR chemical shifts (ppm) for $B_{11}H_{13}OH^{-}$ calculated at the B31LYP/aug-cc-pvdz level of theory. Solvent is CD_3CN.

Atoms		**$B_{11}H_{13}OH^{-}$**	
	Observed [a]	**Observed**[31]	**Calculated** [a]
B1	−14.2	−14.1	−12.4
B2, B3	−23.3	−22.9	−23.6
B4, B6	−10.7	−11.0	−11.8
B5	−40.0	−39.3	−40.6

B7	18.8	18.0	20.6
B8, B11	−29.1	−28.9	−27.2
B9, B10	−9.6	−9.7	−8.1

[a] This work.

REFERENCES

1 F. Zheng, M. Kotobuki, S. Song, M. O. Lai and L. Lu, *J. Power Sources*, 2018, **389**, 198–213.

2 G. M. Sheldrick, *Acta Crystallogr. Sect. A Found. Adv.*, 2015, **A71**, 3–8.

3 G. M. Sheldrick, *Acta Crystallogr. Sect. C Struct. Chem.*, 2015, **C71**, 3–8.

4 O. V. Dolomanov, L. J. Bourhis, R. J. Gildea, J. A. K. Howard and H. Puschmann, *J. Appl. Crystallogr.*, 2009, **42**, 339–341.

5 B. R. S. Hansen, M. Paskevicius, M. Jørgensen and T. R. Jensen, *Chem. Mater.*, 2017, **29**, 3423–3430.

6 F. Han, Y. Zhu, X. He, Y. Mo and C. Wang, *Adv. Energy Mater.*, 2016, **6**, 1501590.

7 R. Asakura, L. Duchêne, R. S. Kühnel, A. Remhof, H. Hagemann and C. Battaglia, *ACS Appl. Energy Mater.*, 2019, **2**, 6924–6930.

8 Z. Lu and F. Ciucci, *Chem. Mater.*, 2017, **29**, 9308–9319.

9 M. Paskevicius, M. B. Ley, D. A. Sheppard, T. R. Jensen and C. E. Buckley, *Phys. Chem. Chem. Phys.*, 2013, **15**, 19774–19789.

10 M. J. Frisch, G. W. Trucks, H. B. Schlegel, G. E. Scuseria, M. A. Robb, J. R. Cheeseman, G. Scalmani, V. Barone, G. a. Petersson, H. Nakatsuji, X. Li, M. Caricato, a. V. Marenich, J. Bloino, B. G. Janesko, R. Gomperts, B. Mennucci, H. P. Hratchian, J. V. Ortiz, a. F. Izmaylov, J. L. Sonnenberg, Williams, F. Ding, F. Lipparini, F. Egidi, J. Goings, B. Peng, A. Petrone, T. Henderson, D. Ranasinghe, V. G. Zakrzewski, J. Gao, N. Rega, G. Zheng, W. Liang, M. Hada, M. Ehara, K. Toyota, R. Fukuda, J. Hasegawa, M. Ishida, T. Nakajima, Y. Honda, O. Kitao, H. Nakai, T. Vreven, K. Throssell, J. a. Montgomery Jr., J. E. Peralta, F. Ogliaro, M. J. Bearpark, J. J. Heyd, E. N. Brothers, K. N. Kudin, V. N. Staroverov, T. a. Keith, R. Kobayashi, J. Normand, K. Raghavachari, a. P. Rendell, J. C. Burant, S. S. Iyengar, J. Tomasi, M. Cossi, J. M. Millam, M. Klene, C. Adamo, R. Cammi, J. W. Ochterski, R. L. Martin, K. Morokuma, O. Farkas, J. B. Foresman and D. J. Fox, *Gaussian 09, Revis. A. 02*, 2009.

11 R. A. Kendall, T. H. Dunning and R. J. Harrison, *J. Chem. Phys.*, 1992, **96**, 6796–6806.

12 A. E. Reed, R. B. Weinstock and F. Weinhold, *J. Chem. Phys.*, 1985, **83**, 735–746.

13 R. Ditchfield, *Mol. Phys.*, 1974, **27**, 789–807.

14 V. Barone and M. Cossi, *J. Phys. Chem. A*, 1998, **102**, 1995–2001.

15 P. Gao, X. Wang, Z. Huang and H. Yu, *ACS Omega*, 2019, **4**, 12385–12392.

16 H. S. Rzepa, S. Arkhipenko, E. Wan, M. T. Sabatini, V. Karaluka, A. Whiting and T. D. Sheppard, *J. Org. Chem.*, 2018, **83**, 8020–8025.

17 E. A. V. Ebsworth and N. Sheppard, *Spectrochim. Acta*, 1959, **13**, 261–270.

18 J. Pecyna, I. Rončević and J. Michl, *Molecules*, 2019, **24**, 3779.

19 M. Bishop, N. Shahid, J. Yang and A. R. Barron, *Dalt. Trans.*, 2004, 2621–2634.

20 Z. Łodziana, P. Błoński, Y. Yan, D. Rentsch and A. Remhof, *he J. Phys. Chem. C*, 2014, **118**, 6594–6603.

21 P. Broadhead and G. A. Newman, *Spectrochim. Acta Part A Mol. Spectrosc.*, 1972, **28**, 1915–1923.

22 D. Sethio, L. M. Lawson Daku and H. Hagemann, *Int. J. Hydrogen Energy*, 2017, **42**, 22496–22501.

23 S. Kim, H. Oguchi, N. Toyama, T. Sato, S. Takagi, T. Otomo, D. Arunkumar, N. Kuwata, J. Kawamura and S. Orimo, *Nat. Commun.*, 2019, **10**, 1–9.

24 M. Matsuo, A. Remhof, P. Martelli, R. Caputo, M. Ernst, Y. Miura, T. Sato, H. Oguchi, H. Maekawa, H. Takamura, A. Borgschulte, A. Züttel and S. I. Orimo, *J. Am. Chem. Soc.*, 2009, **131**, 16389–16391.

25 T. Zhang, Y. Wang, T. Song, H. Miyaoka, K. Shinzato, H. Miyaoka, T. Ichikawa, S. Shi, X. Zhang, S. Isobe, N. Hashimoto and Y. Kojima, *Joule*, 2018, **2**, 1522–1533.

26 R. Asakura, D. Reber, L. Duchêne, S. Payandeh, A. Remhof, H. Hagemann and C. Battaglia, *Energy Environ. Sci.*, 2020, **13**, 5048–5058.

27 W. S. Tang, K. Yoshida, A. V. Soloninin, R. V. Skoryunov, O. A. Babanova, A. V. Skripov, M. Dimitrievska, V. Stavila, S. I. Orimo and T. J. Udovic, *ACS Energy Lett.*, 2016, **1**, 659–664.

28 S. Payandeh, R. Asakura, P. Avramidou, D. Rentsch, Ł. Zbigniew, C. Radovan, A. Remhof and C. Battaglia, *Chem. Mater.*, 2020, **32**, 1101–1110.

29 Y. Sadikin, M. Brighi, P. Schouwink and R. Černý, *Adv. Energy Mater.*, 2015, **5**, 1501016.

30 L. Duchêne, R. S. Kühnel, D. Rentsch, A. Remhof, H. Hagemann and C. Battaglia, *Chem. Commun.*, 2017, **53**, 4195–4198.

31 O. Volkov, K. Radacki, P. Paetzold and X. Zheng, *Zeitschrift für Anorg. und Allg. Chemie*, 2001, **627**, 1185–1191.